The Canadian Mineralogist
Vol. 31, pp. 973-995 (1993)

CHARACTER OF ACTIVE HYDROTHERMAL MOUNDS AND NEARBY ALTERED HEMIPELAGIC SEDIMENTS IN THE HYDROTHERMAL AREAS OF MIDDLE VALLEY, NORTHERN JUAN DE FUCA RIDGE: DATA ON SHALLOW CORES*

ROBERT J.W. TURNER

Geological Survey of Canada, 100 West Pender Street, Vancouver, British Columbia V6B 1R8

DOREEN E. AMES, JAMES M. FRANKLIN and WAYNE D. GOODFELLOW

Geological Survey of Canada, 601 Booth Street, Ottawa, Ontario K1A OE8

CRAIG H.B. LEITCH

Geological Survey of Canada, 100 West Pender Street, Vancouver, British Columbia V6B 1R8

TRYGVE HÖY

British Columbia Ministry of Energy, Mines and Petroleum Resources, Geological Survey Branch, 553 Superior Street, Victoria, British Columbia V8V 1X4

Abstract

The Area of Active Venting hydrothermal field (AAV) occurs within the Middle Valley sediment-filled rift on northern Juan de Fuca Ridge. The AAV is a rhomb-shaped zone of hydrothermally altered sediment 800 m by 350 m with moderate temperature venting (<276°C), associated with anhydrite chimneys on hydrothermal mounds, and biota-rich areas associated with diffuse venting. Ten push-core samples (< 30 cm depth) were collected in and near the AAV by the submersible ALVIN during 1990 to examine the surficial nature of altered hemipelagic sediment and hydrothermal mounds. Within the AAV but away from active vent areas, weakly altered sediment is grey colored and indurated due to dissolution of calcareous microfossils and an increase in authigenic calcite and pyrite. Proximal to vent areas, intensely altered sediment is green colored, with an increased abundance of Mg-smectite, iron-bearing illite–smectite, pyrite, organic carbon and barite. Altered sediments contain elevated contents of MgO, total Fe_2O_3, MnO, S, Ba, Zn, Cu, Pb, As, Sb and Se, and are depleted in CaO and CO_2 relative to unaltered sediment. Element enrichments and depletions increase toward active vent areas on hydrothermal mounds. Tilted hydrothermal crusts, and horizontal Mg-silicate veins seen in the cores, suggest that hydrothermal mounds grow by inflation, whereas chimney growth and collapse contribute a veneer of hydrothermal sediment. Sediment adjacent to an active chimney has layers of anhydrite, sulfide and nodular Mg-silicate. The sediment contains a high content of MgO and reduced S, and is composed of serpentine, saponite, talc, pyrrhotite, pyrite, gypsum, anhydrite, marcasite, sphalerite, chalcopyrite, isocubanite and galena. The upper layer reflects recent chimney collapse, whereas the sulfide layer represents a residual accumulation of past collapse events. The abundance of Mg-silicates and limited biota suggest that recharge occurs over much of the mound surface, whereas discharge is focused at chimneys. Hydrothermal sediments in areas of diffuse venting are characterized by strong H_2S odor, abundant quartz, amorphous silica, barite, smectite, organic matter and biota. They differ from mound sediments by higher contents of Ba and SiO_2, and lower contents of S and most chalcophile elements. These areas may represent an incipient stage of hydrothermal mound growth.

Keywords: Juan de Fuca Ridge, Middle Valley, sediment-filled rift, hydrothermal mound, sediment alteration, seafloor.

---

* Geological Survey of Canada contribution number 35693.

Sommaire

Le champ d'activité hydrothermale dit "Area of Active Venting" est situé au sein de Middle Valley, une zone de rift remplie de sédiments dans le secteur nord de la crête de Juan de Fuca. Dans ce secteur rhombique, 800 m de long et 350 m de large, où affleurent des sédiments modifiés par activité hydrothermale, se trouvent des évents à température moyenne (<276°C) associés avec des cheminées à anhydrite et des amoncellements de débris hydrothermaux, ainsi que des zones riches en activité biologique où les évents sont plus diffus. Dix échantillons de carottes obtenus par pénétration forcée (<30 cm de profondeur) ont été prélevés près de cette zone avec l'aide du sousmarin ALVIN en 1990, dans le but d'examiner la surface des sédiments hémipélagiques altérés, ainsi que les amoncellements hydrothermaux. A une certaine distance des évents actifs, les sédiments ne sont que faiblement altérés; ils sont gris, et endurcis à cause de la dissolution des microfossiles riches en carbonate et de la déposition de calcite authigène et de pyrite. Plus près des évents, les sédiments, devenus verts, sont plus fortement altérés, avec une concentration accrue d'un membre magnésien du groupe de la smectite, une argile interstratifiée à illite–smectite, pyrite, carbone organique, et baryte. Ces sédiments altérés contiennent des teneurs élevées de Mg, fer total, Mn, S, Ba, Zn, Cu, Pb, As, Sb et Se, et sont appauvris en Ca et en CO_2 par rapport au précurseur. Ces tendances d'enrichissement et d'appauvrissement augmentent en intensité vers les évents actifs situés sur les amoncellements hydrothermaux. Les segments de croûte basculés, et la présence de veines horizontales à silicates de Mg repérées dans les carottes, font penser que ces amoncellements croissent par gonflement, tandis que la croissance et l'affaissement des cheminées contribuent une mince couche de sédiments hydrothermaux. Les sédiments près des évents contiennent des couches d'anhydrite, de sulfures et de silicate magnésien en nodules. Ces sédiments sont enrichis en Mg et en soufre réduit, et sont faits de serpentine, saponite, talc, pyrrhotite, pyrite, gypse, anhydrite, marcasite, sphalérite, chalcopyrite, isocubanite et galène. La couche supérieure contient les débris dus à l'affaissement récent de cheminées, tandis que la couche de sulfures représente une accumulation résiduelle due à des affaissements antérieurs. D'après l'abondance de silicates magnésiens et la présence restreinte d'activité biologique, la zone de recharge du système serait diffuse sur une grande partie de la surface de l'amoncellement; la zone de décharge, par contre, est centrée sur les cheminées. Les sédiments hydrothermaux des zones à décharge plus diffuse ont une forte odeur de H_2S, et montrent une abondance de quartz, silice amorphe, baryte, argile smectitique, matière organique et activité biologique. Ils diffèrent des sédiments typiques des amoncellements par leur concentration en Ba et en SiO_2, et leur appauvrissement en S et la plupart des éléments chalcophiles. Ces zones pourraient représenter un stade précoce du cycle de développement d'un amoncellement hydrothermal.

(Traduit par la Rédaction)

Mots-clés: crête de Juan de Fuca, Middle Valley, rift rempli de sédiments, amoncellement hydrothermal, altération de sédiments, fonds océaniques.

Introduction

Hydrothermal centers along sediment-free spreading ridges reflect the direct interaction between hydrothermal fluid of seawater origin and mid-ocean ridge basalt. However, where spreading ridges are blanketed by thick sediment, the geothermal system and hydrothermal fluid are modified by the physical and chemical properties of the pile of sediments. In the eastern Pacific, several spreading centers occur close to the North American continental margin and are covered by significant thicknesses of turbidite and hemipelagic sediment. Areas of hydrothermal activity and massive sulfide deposits have been discovered in sediment-covered rifts at Guaymas Basin in the Gulf of California (Lonsdale & Becker 1985, Koski *et al.* 1985), Escanaba Trough on southern Gorda Ridge (Koski *et al.* 1988), Middle Valley of the northern Juan de Fuca Ridge (Goodfellow & Blaise 1988), and Hess basin, Galapagos Rift (Honnorez *et al.* 1981).

Middle Valley is a sediment-covered failed rift near the intersection of the Endeavour segment of the Juan de Fuca Ridge and the Sovanco Fault, about 300 km west of the continental margin of British Columbia and Washington (Fig. 1). Early work recognized discrete areas of high heat flow, sulfide deposits and altered sediments within the rift valley (Davis *et al.* 1985, 1987, Goodfellow & Blaise 1988). During 1990 and 1991, a large hydrothermal field, the Area of Active Venting (AAV), and a sulfide mound area were mapped and sampled using the ALVIN submersible (Ames *et al.* 1993). Leg 139 of the Ocean Drilling Project completed a series of holes in Middle Valley, including the AAV hydrothermal field and a large sulfide deposit (Davis *et al.* 1992).

This study utilizes push-core samples (<30 cm depth) collected during the 1990 dive program by the submersible ALVIN to examine the nature of surficial alteration of hydrothermal mounds and surrounding sediment within the AAV hydrothermal field. Push cores deployed by a submersible give an excellent undisturbed record of the shallowest sediments and allow well-located sampling of specific features on the seafloor. On the basis of data on pore water from piston and gravity cores, Lydon *et al.* (1992) indicated that hydrothermal fluids are moving advectively through the sediments below the AAV hydrothermal field in Middle Valley. This work investigates the surficial zone (<30 cm depth) within the hydrothermal field to study processes of alteration that are operating at and near the sediment–water interface, where thermal gradients are highest, and

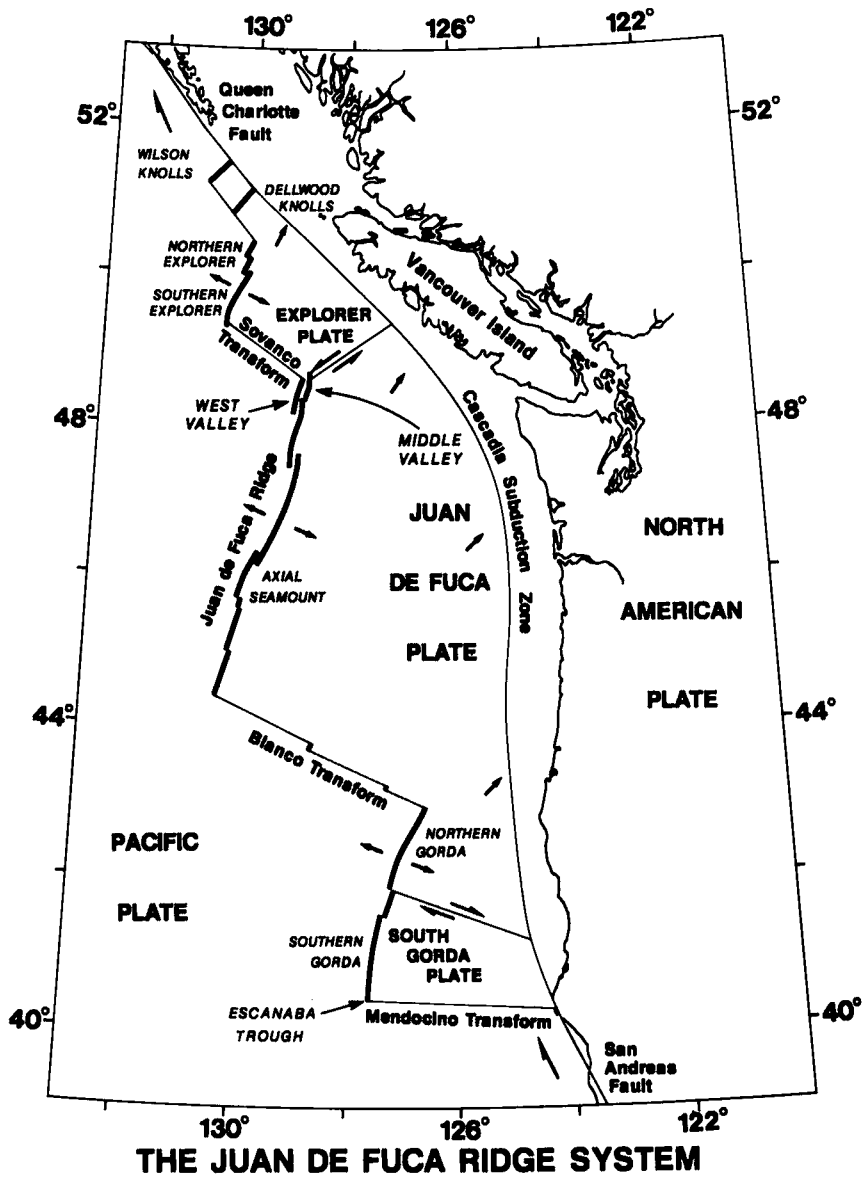

FIG. 1. Map of the Juan de Fuca ocean-ridge system, showing the location of Middle Valley.

where precipitation from the advecting hydrothermal fluid is significant. Other studies presented in this volume address the clay mineralogy (Percival & Ames 1993) and mineralogy and geochemistry (Ames *et al.* 1993) of hydrothermal mounds, and the nature of alteration in shallow sediment (<11.5 m) in and around the hydrothermal fields (Goodfellow *et al.* 1993).

GEOLOGY AND HYDROTHERMAL AREAS WITHIN MIDDLE VALLEY

Most of the Juan de Fuca Ridge is a high-standing ridge free of sediment. Near the north end of Endeavour segment, adjacent to the Sovanco Transform, however, the ridge is bathymetrically low

and partly filled with turbidites derived from the nearby North American continental margin. This northern portion is a double rift that includes West Valley, the current neovolcanic zone of the northern Endeavour segment, and Middle Valley, an older spreading center (Fig. 1). Spreading jumped westward from Middle Valley to its present site in West Valley between two hundred thousand and several tens of thousands of years ago (Davis & Lister 1977, Karsten *et al.* 1986).

Middle Valley is about 10 km wide and lies at a depth of 2350 to 2500 m below mean sea level. Acoustic imagery and Seabeam bathymetry indicate that the valley is bound on the east by north-trending faults that elevate blocks of basaltic crust with a thin overlying cover of sediment (Shipboard Scientific Party 1992a). Half of a rifted elongate volcano forms the western margin. The valley has a prominent medial fault, with sediments on the western side down-thrown relative to those to the east. Seismic data indicate that abundant faults cut the sediment fill underlying the valley. The central part of the valley consists of over 960 meters of sediments and gabbroic sills. The section thickens northward to the Sovanco Transform (Davis *et al.* 1987). The sills form about 40% of the section below 500 m below seafloor (Shipboard Scientific Party 1992b). The eastern half of Middle Valley contains over 15 prominent hills, each typically 400 m in diameter and 30–50 m high. One of these is underlain by picritic intrusions (ODP Site 856), and is adjacent to a very large massive sulfide deposit. In addition, three areas of active venting have been noted. The most southerly of these is a single vent emanating from a prominent mound of massive sulfide, about 300 m south of Bent Hill (inset, Fig. 2). A second area of venting has been mapped about 1 km south of the "Area of Active Venting" or AAV. The AAV contains over twenty vent-sites, as described below.

Area of Active Venting

The Area of Active Venting (AAV) is situated on an uplifted sediment-covered plain just east of a shallow west-facing bathymetric scarp underlain by west-side-down faults (Goodfellow & Blaise 1988, Goodfellow *et al.* 1993). A rhomb-shaped acoustic reflector (Fig. 2) that indicates the extent of hydrothermally indurated sediment extends 800 m north–south and 350 m east–west. The AAV occurs above a buried basalt "hill" of similar dimension intersected at 260 m below seafloor by ODP Hole 858F (Davis *et al.* 1992). Chemical data (Davis *et al.* 1992) indicate that the basalt has an affinity with seamounts in the Pacific Plate. The eastern margin of the acoustic reflector is coincident with a fault that extends to the south to another area of venting described above (Johnson *et al.* 1990).

Hydrothermal mounds with associated active and inactive chimneys and rubble occur throughout the AAV, but are most prominent in the northern and southern thirds. Mounds are typically about 15 m in diameter, but composite mounds such as in the Chowder Hill area (Fig. 2) are as much as 50 m in width. Mounds vary from about 2 to 15 m in height. Each mound is flanked by an apron of partially indurated, rough-textured sediment. Rubble blocks are angular, and typically 20–30 cm in diameter. The slopes of the mound vary from 10 to 30°, and are composed of indurated sediment, displaced slabs of indurated sediment, and sedimentary rubble. Bacterial mats cover areas of a few square meters near the top of many mounds. On top of each mound, and less commonly on the upper part of the slope, are actively venting chimneys. Each vertically standing anhydrite–pyrite chimney, from 0.5 to 9 m high, is surrounded by an apron of anhydrite rubble and fine sediment. Active chimneys and hydrothermal crusts from mound surfaces are sulfide-poor and composed of anhydrite, gypsum, bassanite, barite, silica, Mg-rich silicate and pyrite, with lesser marcasite, pyrrhotite, chalcopyrite, sphalerite and galena (Ames *et al.* 1993). Temperatures of venting fluids were found to be between 184 to 276°C. Inactive chimneys occur on the flanks of some mounds; these are composed primarily of barite, with significant hydrocarbon material (Ames *et al.* 1993).

Biological activity is largely confined to the flank and basal areas of the mounds. Sparse tube-worm colonies, clam beds, and bacterial mats are most common, with galatheid crabs also present. The biological abundance appears to be controlled by availability of heat. A series of heat-flow measurements taken along a traverse of push-core sites (*i.e.*, 2254) indicate that the subseafloor temperature increases toward the mound, reaching a maximum at the base (H.P. Johnson, pers. comm. 1990). The flanks of the mound are relatively cool.

Coincident with the area of maximum biological activity are hummocky areas of diffuse venting. This was particularly evident in the Heineken Hollow area near the north end of the AAV, but also was observed near both Dead Dog and Chowder hills. In a clam bed near the latter area, the temperature was 12°C at a depth of only 4 cm.

During Leg 139 of the Ocean Drilling Program in 1991, drilling at the AAV (Site 858) intersected altered sediment but not massive sulfides (Shipboard Scientific Party 1992c), suggesting that the AAV has been a center of lower-temperature hydrothermal discharge throughout its history. Sediments underlying the AAV have been altered to central chlorite – albite – quartz and zeolite – quartz assemblages flanked by anhydrite – clay and outer calcite – clay (Shipboard Scientific Party 1992c). The chlorite – albite – quartz assemblage is associated with veins, fractures and breccias.

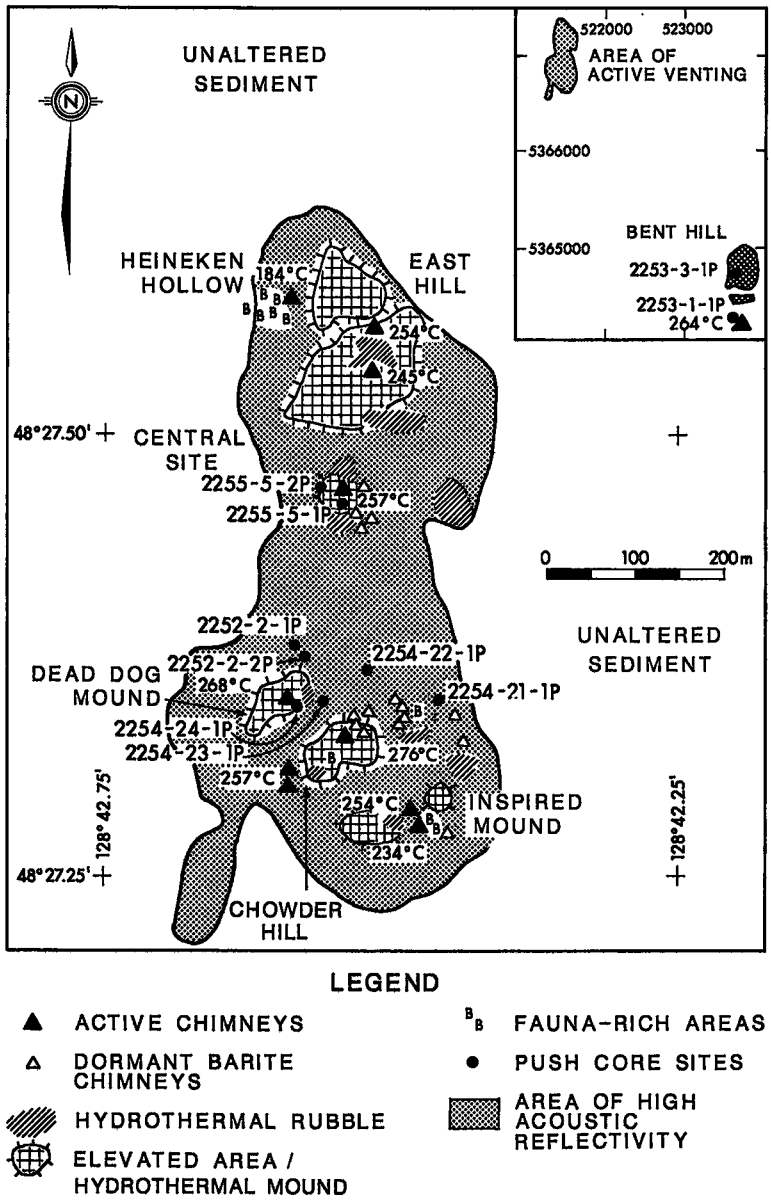

FIG. 2. Map of Area of Active Venting, based on visual observations from ALVIN dives and acoustic imagery mapping. Inset map shows location of Area of Active Venting northwest of Bent Hill seafloor knoll and hydrothermal mound south of Bent Hill. The locations of push-core samples are noted on the two maps.

Bent Hill hydrothermal area

Bent Hill (Fig. 2, inset) is an uplifted and east-tilted block of partially indurated sediment. Its western margin is a fault scarp, with considerable sediment "talus" at its base. The hill is segmented into a series of elongate north–south blocks, each bound by a fault. Immediately south of Bent Hill is a prominent mound of massive sulfide, about 35 m high and over 100 m in diameter. Massive sulfide was cored to a depth of 95 meters below seafloor (ODP, Hole 856 H). The upper few meters of the deposit consist of sulfide

rubble (Goodfellow & Blaise 1988), but for the most part, the deposit is not bedded. It is composed primarily of pyrite and pyrrhotite, with abundant magnetite locally. It contains about 3% Zn, 0.5% Cu, less than 75 ppm lead, and only a trace of barite. The sulfides are recrystallized, and the metals are interpreted to have been redistributed during later lower-temperature hydrothermal activity.

The vent area south of Bent Hill is quite different from those in the AAV. Hydrothermal fluids (264°C) are emanating from a single chimney at the top of a mound of massive sulfide. This mound is about 50 m in diameter, and 15 m high. Blocks of massive sulfide rubble occur on its flank and around its base (Ames *et al.* 1993). The sulfides are similar to those at the Site 856 sulfide deposit, and are not forming at present. They may, however, be undergoing modification by the present hydrothermal activity. The anhydrite chimney is similar to chimneys on mounds in the AAV, surrounded by an anhydrite apron.

Sampling and Analytical Methods

Push cores were collected during five dives with the submersible ALVIN during 1990. Sample numbers used in this report (*e.g.*, 2252–2–1) are composed of three parts that represent the dive number, site number on that dive, and sample number at that site. At each push-core site, the push corer was inserted to a depth of 30 cm, with the core stored in a receiving tube in order to prevent washing of the material. Samples were curated and split onboard ship. Each was logged and sampled, with samples taken for pore-water recovery. Samples and core were sealed and kept in refrigerated storage. At each push-core site, temperature data were taken using a 1-m-long heat probe.

Transmitted and reflected light petrography, and a Philips PW 1710 X-ray diffractometer operating at 50 kV and 30 mA and emitting Cu$K\alpha$ radiation, were used for mineral identification of bulk samples. For X-ray-diffraction (XRD) studies, samples were washed with distilled water three times to remove salt. A clay-sized (<2 μm) fraction was separated by centrifuge and analyzed by X-ray diffraction. Chemical dispersants such as sodium metaphosphate that might alter the clay compositions were not utilized during centrifugation. Smear mounts of the bulk and clay-sized fraction were analyzed by XRD while air-dried, and after saturation with ethylene glycol and heat treatment to 550°C to determine the presence of expandable, non-expandable and mixed-layer clay minerals. Smectite was identified on the diffractometer trace by its expansion to 17 Å after glycol treatment combined with collapse to 10 Å after heating to 550°C for two hours. Mg-rich smectitic material was identified by further SEM and electron-microprobe studies. Illite–smectite mixed-layer minerals were identified by the presence of a shoulder on the low-Å side of the 001 illite peak (10.1 Å), as well as the partial expansion to 17 Å upon glycolation and collapse to 10 Å upon heating. Follow-up electron-microprobe studies identified an iron-bearing illite–smectite mixed layer mineral. A smectite–chlorite mixed-layer mineral was recognized by collapse to between 10 and 14 Å during heating (typically 12.5 Å). Mg-(Fe) chlorite was distinguished from Fe-(Mg) chlorite by a greater intensity of the 14-Å peak when air dried.

In a detailed clay study on the active chimneys and a push core from the Central Site hydrothermal mound, Percival & Ames (1993) determined the presence of saponite, serpentine and either a physical mixture of saponite and serpentine or a saponite–serpentine mixed-layer mineral. Techniques used to determine these minerals are those described above (XRD, electron microprobe, SEM), with the addition of analytical transmission electron microscopy (ATEM). Push cores from two hydrothermal mounds are described in this paper, but only one (Central Site mound, core 2255–5–1) has been studied with the ATEM and electron microprobe; at the Bent Hill mound, XRD analyses of the clays could only determine the group name, and hence the term Mg-rich smectite is used. Therefore, both "saponite" and "Mg-rich smectite" are used in the discussion of the hydrothermal mounds.

Qualitative analysis and imaging of the fine-grained clays and sulfides in polished thin sections and fragment mounts were conducted on a Cambridge S–200 scanning electron microscope (SEM) with an integrated Link Analytical AN10,000 energy-dispersion X-ray analyzer at the Geological Survey of Canada, Ottawa. The composition of the clay minerals was obtained from polished thin sections using a CAMEBAX wavelength-dispersion electron-microprobe with attached energy-dispersion X-ray analyzer, using a 10-μm beam diameter and an accelerating voltage of 15 kV. A computer program developed by the Geological Survey of Canada (G. Pringle, pers. comm., 1992) was utilized to calculate the formulae of the clay minerals, and the excess charges were determined according to Moore & Reynolds (1989).

Cores that were analyzed for bulk chemical composition were sampled continuously at 4- to 16-cm intervals. Each sample was oven dried at 110°C, pulverized and ground to –200 mesh, and analyzed at the Geological Survey of Canada after fusing 0.5 g of sample with lithium metaborate and dissolving the fused sample in 5% HNO_3. The analytical methods are: Induction Coupled Plasma – Emission Spectrometry: SiO_2, TiO_2, Al_2O_3, K_2O, Na_2O, CaO, MgO, P_2O_5, MnO, Fe_2O_3(total), Zn, Cu, Pb, Ba, Mo, Sr, Rb, Be, Co, Cr, La, Nb, Ni, V, Y, Yb and Zr; Atomic Absorption Spectrometry: As, Sb, Se; combustion and wet-chemical methods: FeO, H_2O, CO_2, organic C and S.

Geology of Push-Core Samples

Eight push cores were collected in the AAV, two in the area around Bent Hill (Turner *et al.* 1991; Fig. 2). In the AAV, all cores were taken from within the area of high acoustic reflectance that encloses the vents, in order to examine the distribution of alteration and hydrothermal minerals. Most cores were taken near vent sites, including an area of diffuse venting, a mound top, and talus flanking a mound (Fig. 3). The series of cores on dive 2254 were taken along a traverse that approached Dead Dog mound from the east. These core sites are spaced away from the Dead Dog vent site, from site 2254–21 near the eastern margin of the acoustic reflector, to site 2254–24, within about 1 m of the hydrothermal mound (Fig. 2). The two cores in the Bent Hill area were taken on top of a sulfide mound adjacent to a venting chimney, as well as on top of Bent Hill (2253–3–1). The latter site is the furthest away from any form of past or present venting, and is the least altered core (Fig. 2, inset).

Goodfellow & Blaise (1988) and Goodfellow *et al.* (1993) have divided the shallow sediments in Middle Valley into an upper hemipelagic mud unit, a middle turbidite unit and a lower hemipelagic mud unit. The upper hemipelagic mud unit varies from 2 to 4 m in

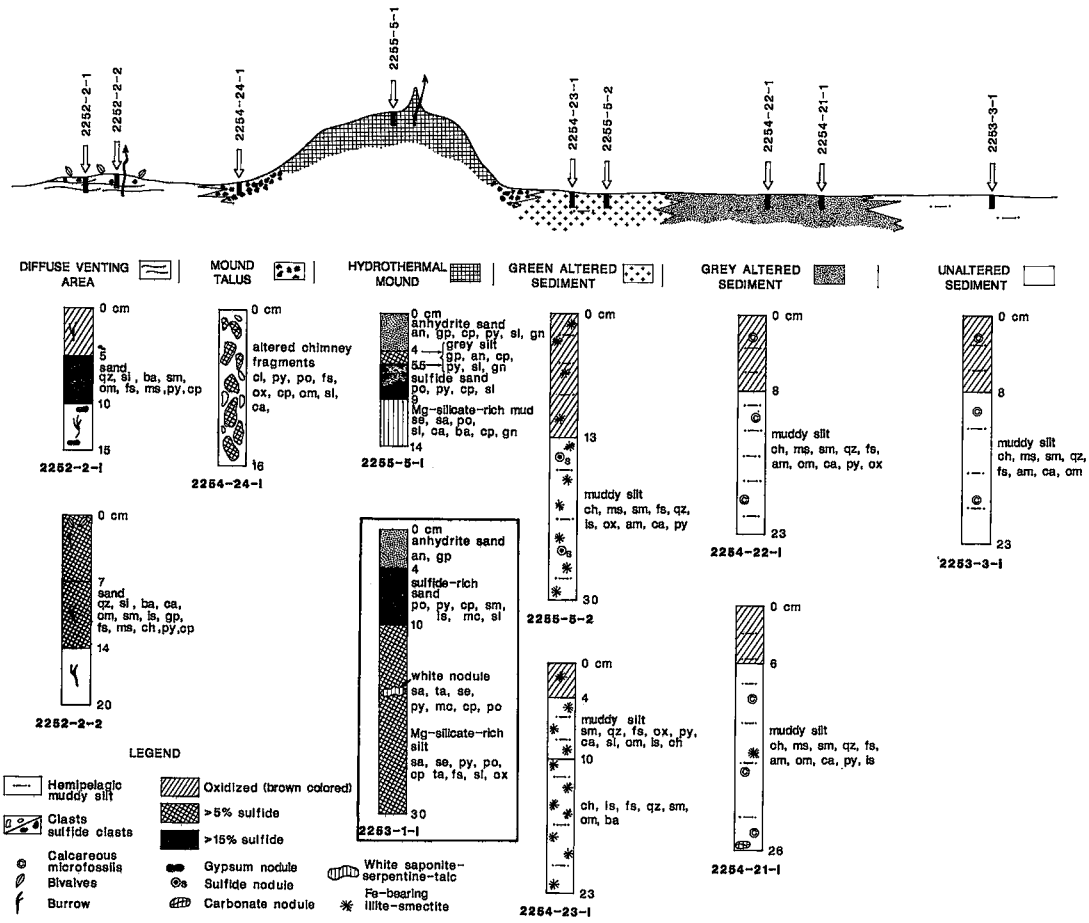

FIG. 3. Graphic logs displaying texture, stratigraphy and mineralogy of push-core samples. Cores are from the AAV except core from sulfide mound south of Bent Hill (in box) and unaltered sediment core. Cores are shown in approximate position with respect to schematic profile of a hydrothermal mound and adjacent sediment (modified after Turner *et al.* 1991). Minerals are listed in order of decreasing abundance. Abbreviations: amphibole (am), anhydrite (an), barite (ba), calcite (ca), chlorite (ch), chalcopyrite (cp), feldspar (fs), galena (gn), gypsum (gp), illite–smectite (is), marcasite (mc), mica (ms), organic matter (om), Fe–Ti oxides and hydroxides (ox), pyrrhotite (po), pyrite (py), quartz (qz), saponite (sa), serpentine (se), amorphous silica (si), sphalerite (sl), smectite (sm), talc (ta).

thickness and is a silty clay rich in foraminifera, diatoms and radiolaria. All push-core samples of altered and unaltered sediment were taken within the upper hemipelagic mud unit. The uppermost sediment, to a depth of 8 cm, is oxidized to a red- or orange-brown color. Average rates of sedimentation for this upper mud unit range from 5.5 to 11.8 cm/ka (Goodfellow & Blaise 1988).

Altered hemipelagic sediment

The cores from the sample transect toward Dead Dog Mound (2254–21/22/23) within the acoustically reflective area of the AAV show a change from an outer grey-colored altered sediment ("grey-altered sediment") to a green-colored alteration near the hydrothermal mound ("green-altered sediment") (Fig. 3). Grey-altered sediment is similar in color to olive-grey unaltered sediments but is distinctly more indurated. The 2254–21 core site lies near the edge of the acoustic reflector near a north-trending cluster of dormant barite-bearing chimneys (Fig. 2). The 2254–22 core site is located on the northern margin of the Dead Dog – Inspired vent complex (Fig. 2). The seafloor in this area is a flat sedimented plain without chimney structures or sulfide rubble near the sample site. Several attempts were required to collect a push core owing to the indurated nature of the sediment.

Green-altered sediment is noted up to 40 m from hydrothermal mounds and is distinguished from normal olive grey sediment by a distinctive green color and increased sulfide content (Fig. 3). Green-altered sediment was penetrated at two sites, approximately 40 m from the Dead Dog hydrothermal mound on a flat sediment plain adjacent to an inactive barite chimney, rubble and dead tubeworms (2254–23–1), and less than 15 m from the base of the hydrothermal mound, at the Central site vent complex (2255–5–2).

Talus rubble on flank of mound

A talus deposit flanking the Dead Dog hydrothermal mound in the southern Dead Dog – Inspired hydrothermal area of the AAV was sampled by core 2254–24 (Figs. 2, 3). The coarse, well-sorted gravel of grey–green-altered fragments (up to 5 cm across) represents material slumped from the adjacent mound. Some debris, such as tube-shaped fragments with crystals radial about a central orifice, appear derived from hydrothermal chimneys.

Sediment-filled depressions on hydrothermal mounds

A hydrothermal mound at the Central Site in the AAV, as well as the sulfide mound south of Bent Hill, were sampled by push cores (sites 2255–5–1, 2253–1–1) (Fig. 2). Both cores sampled aprons of fine-grained hydrothermal sediment adjacent to active anhydrite-bearing chimney structures (257 and 264°C). The Central Site core penetrated a toppled chimney overlying the sediment.

Both cores contain a similar stratigraphy: an upper anhydrite-rich layer, an underlying sulfide-rich layer, and a lower Mg-silicate-rich layer (Fig. 3). The upper anhydrite-rich layer is the "snow cap" sediment observed by ALVIN as surrounding or adjacent to hydrothermal chimneys. The underlying sulfide-rich layers are 3.5 and 6 cm thick. The sulfide-rich layers have a sharp basal contact and slightly gradational upper contact. Black fine-grained sulfide–anhydrite clasts up to 1.5 cm diameter occur just above the base of the sulfide layer at the AAV mound. This sulfide-rich layer has similar mineral textures to mound chimneys (Ames *et al.* 1993). The lowest layer in each core (>10 cm depth) is dominated by Mg-silicate minerals. In the longer Bent Hill core (2253–1–1), dark grey sandy silt with disseminated fine-grained sulfide of the lower layer contains white soft nodules up to 3 cm across. The AAV core (2255–5–1) intersected 5 cm of massive white clay nodule cut by subhorizontal, bifurcating veins of similar material.

Areas of diffuse hydrothermal discharge

Immediately northeast of the Dead Dog hydrothermal mound area, within the AAV, is a hummocky area several meters in diameter, with shimmering waters due to diffuse discharge of hydrothermal fluids. Sediment recovered in two cores (site 2252–2; Fig. 2) is layered, partially indurated, and greenish grey to dark grey in color. Sediment layers 5–7 cm thick are distinguished by changes in color. In contrast with all other sediments sampled, these sediments are characterized by strong H_2S odor, and an abundance of amorphous silica, barite, organic matter, and biota. Shell fragments including *Calyptogena* are common in the uppermost sediment, and sulfide-encrusted siliceous casts of polychaete worm burrows, one of which was inhabited by an obellid polychaete worm (M. Black, pers. comm. 1990), occur throughout both cores. The worm burrows are up to 5 mm diameter and commonly have a branching form.

Mineralogy

Goodfellow & Blaise (1988) reported that bulk samples of hemipelagic and turbiditic sediment contain quartz, plagioclase, amphibole, mica, chlorite, as well as calcareous and siliceous microfossils. The <2 μm fractions contain smectite, chlorite, illite, irregular mixed-layer clays, feldspar, amphibole and quartz. At core site 2253–3–1, we recovered unaltered sediment composed of chlorite, illite, illite–smectite, quartz, and smectite, and contains scattered coarser grains of foraminifera, radiolaria, diatoms, quartz, feldspar, amphibole and pyrite (Figs. 3, 4).

Altered sediment

Grey-altered sediment is composed of chlorite, clay, and muscovite, with scattered silt-size grains of quartz, plagioclase, foraminifera, siliceous microfossils and amphibole (Figs. 3, 4, 5). The clay-sized fraction is dominated by chlorite and quartz, with minor plagioclase and mica and trace amounts of an illite–smectite mixed-layer phase, smectite and amphibole (Figs. 3, 5g, h). This altered sediment is distinguished from unaltered sediment by a marked decrease in abundance of foraminifera, with an increase in authigenic calcite and pyrite causing the indurated nature of grey-altered sediment (Fig. 4). Pyrite occurs as small patches of very fine euhedral grains (50–150 μm), as framboidal grains, and as local replacements of foraminifera tests (Fig. 5h).

Green-altered sediment consists of an iron-bearing illite–smectite mixed-layer mineral, Mg-rich smectite, Mg-rich chlorite, chlorite–smectite mixed-layer mineral, illite, quartz, plagioclase, amphibole, barite, amorphous silica, radiolaria, and diatoms (Figs. 3, 5e, f). Green-altered sediment is distinguished in mineral content from grey-altered sediment by the marked increase in abundance of Mg-rich smectite, iron-bearing illite–smectite, and pyrite, the presence of barite, and increased abundance of organic carbon (Fig. 4). The distinction between detrital and authigenic clay minerals is most obvious where there is clear textural evidence of coating and replacement (Figs. 6b, d). Iron-bearing illite–smectite and Mg-rich smectite occur as 10–15 μm aggregates that replace anhydrite crystals, surround lath-shaped voids (Fig. 6b), and form irregular clots (50–100 μm) in a silica-rich matrix (Fig. 6d). Iron-bearing illite–smectite patches increase in abundance with depth and give the core a distinctive green color. The MgO/(MgO+FeO) ratio of chlorite in the green-altered sediment is greater than that of chlorite in the grey-altered sediment. Mg-rich smectite in the green-altered

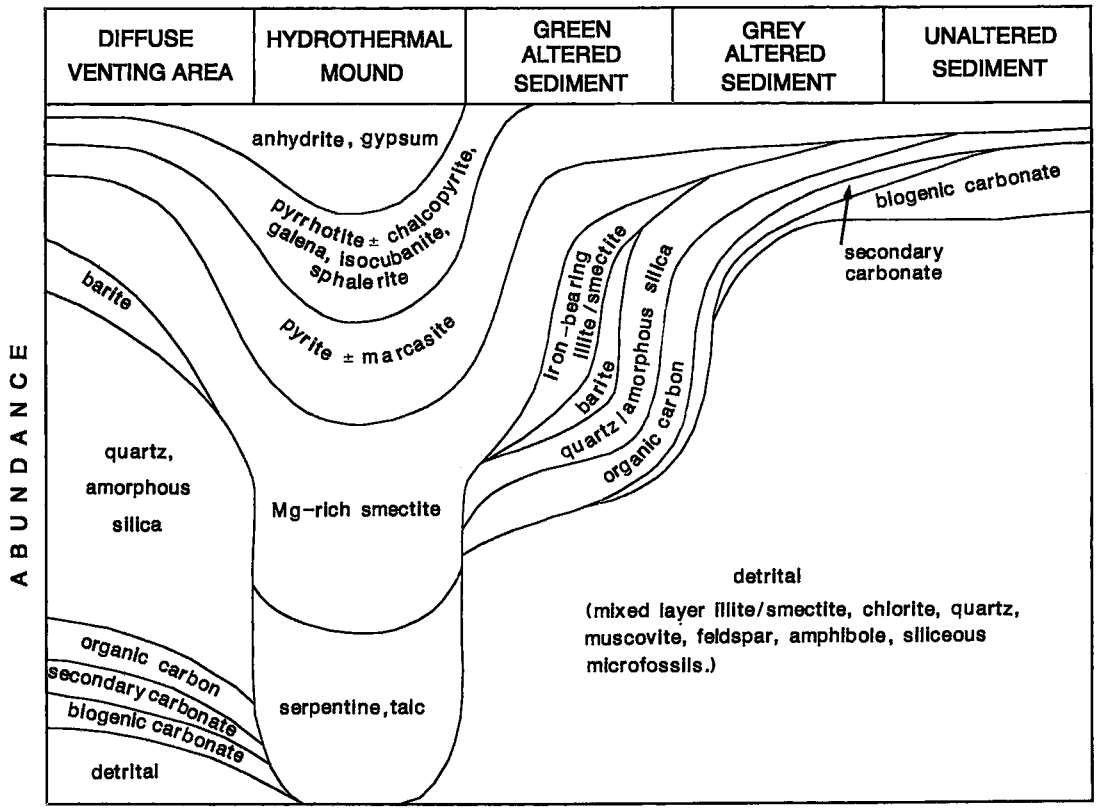

FIG. 4. Schematic diagram showing mineral content of shallow material in hydrothermal mounds, areas of diffuse venting, altered sediments proximal and distal to hydrothermal mounds, and unaltered hemipelagic sediments. Abundances are approximate and based on results of petrographic, SEM and electron-microprobe analyses of push-core materials.

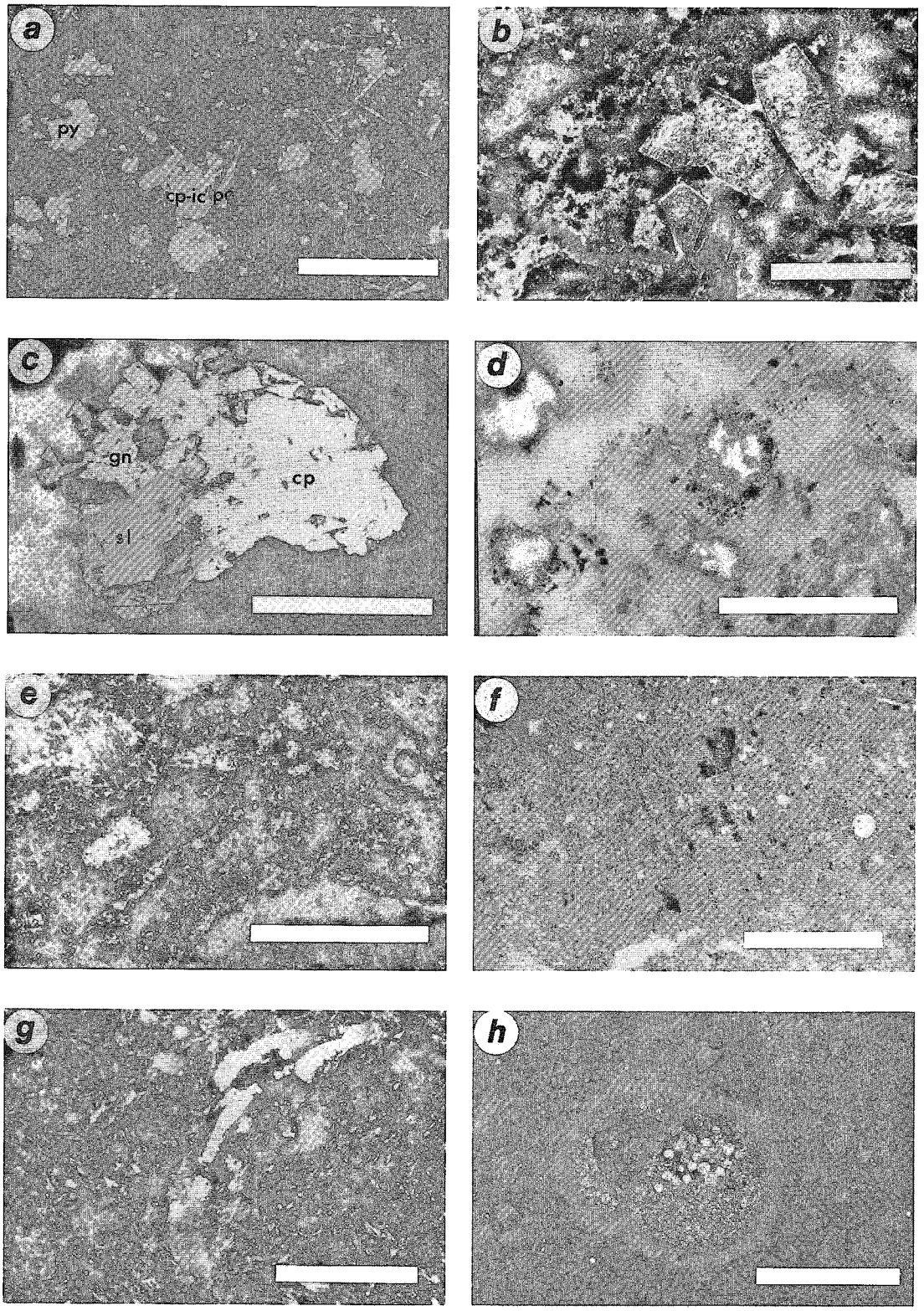
a
py
cp-ic
b
c
gn
cp
sl
d
e
f
g
h

sediment has a lower $MgO/(MgO+SiO_2)$ ratio than Mg-rich smectite in the hydrothermal mounds or area of diffuse venting (Table 1). Barite occurs as clots and rosettes in open spaces (Fig. 6b). Secondary quartz overgrows siliceous fossils and surround aggregates of authigenic clay minerals (Fig. 6c). Pyrite is abundant as disseminated framboids, and as diffuse patches up to 2 cm across of fine-grained disseminated pyrite and chalcopyrite. Irregular nodules of coarse anhydrite occur in the upper oxidized zone.

Sediment-filled depressions on hydrothermal mounds

Cores that sampled hydrothermal mound sediment contain gypsum, serpentine, saponite, and a mixed-layer saponite–serpentine mineral (Percival & Ames 1993; Table 1), sulfides, talc and anhydrite. Pyrrhotite and pyrite are the dominant sulfide minerals, and marcasite, sphalerite, chalcopyrite, isocubanite and galena are present (Fig. 5c). The typical components of hemipelagic sediment, such as detrital quartz, plagioclase, amphibole, chlorite, foraminifera and diatoms, are absent (Fig. 4).

The upper anhydrite-rich layer contains anhydrite, gypsum, silica, pyrite, chalcopyrite, sphalerite and galena. Rims of covellite around chalcopyrite indicate oxidation related to late, lower-temperature hydrothermal alteration, or supergene processes on the seafloor. The upper layer is similar in mineral content to the toppled chimney composed of gypsum, anhydrite, pyrite, sphalerite, chalcopyrite, and smectite (Fig. 5b). The underlying sulfide-rich layers are composed predominantly of fine-grained pyrrhotite, pyrite, saponite and gypsum, with lesser chalcopyrite, marcasite and sphalerite (Fig. 5a). Pyrrhotite, partially replaced by lepidocrocite, occurs as randomly oriented laths with sphalerite and chalcopyrite. Locally, pyrrhotite laths are partly replaced by pyrite and marcasite. Mg-rich smectite occurs as aggregates up to 1 mm, as rims in voids of dissolved anhydrite laths, and as a fine-grained matrix to pyrrhotite laths, interstitial chalcopyrite and sphalerite (Fig. 6a). The lower layers in each core (<10 cm depth) are dominated by saponite, talc, illite and a serpentine-group mineral (Percival & Ames, 1993), and also contain variable amounts of chalcopyrite, galena, pyrite, pyrrhotite, marcasite, sphalerite, barite, calcite and isocubanite (Fig. 5c). Hydrothermal clay in the mounds has a lower silica content and higher $MgO/(MgO+SiO_2)$ ratio and Al content than that in the diffuse venting areas or altered sediment adjacent to mounds (Table 1). The sulfide assemblage in the lower Mg-silicate layer is distinct from the overlying sulfide layer by a higher proportion of base metal to iron sulfides, and a coarser grain-size.

The talus gravel at the base of Dead Dog mound is composed of smectite, pyrite and calcite. Smectite commonly replaces crystal aggregates and occurs as platelets coated with pyrite (Fig. 5d).

Areas of diffuse hydrothermal discharge

The sediment is composed of varying amounts of quartz, amorphous silica, barite, gypsum, pyrite, pyrrhotite, quartz, plagioclase, mica, and minor illite, smectite and illite–smectite mixed layer clays (Figs. 3, 4). The total detrital component (quartz, plagioclase and chlorite) is subordinate to the hydrothermal mineral component, on the basis of petrographic and XRD studies; TiO_2 and Al_2O_3 analyses for these

FIG. 5. Microphotographs of materials from hydrothermal mounds and adjacent altered hemipelagic sediment. (a) Sulfide-rich layer, hydrothermal mound, Bent Hill area. Bladed pyrrhotite (po), euhedral pyrite (py), rounded mass of chalcopyrite–isocubanite (cp–ic), rare sphalerite (sl) in matrix of clay and minor saponite (2253–1–1P, 4 cm depth; reflected plane-polarized light). Scale bar is 100 μm. (b) Material from a collapsed anhydrite chimney, hydrothermal mound, AAV. Euhedral pseudomorphs of gypsum or bassanite after anhydrite, in sulfide–gypsum matrix (2255–5–1, 3 cm depth; transmitted light, crossed polars). Scale bar is 2 mm. (c) Massive white saponite–clay layer, hydrothermal mound, AAV. Grain of coarse chalcopyrite (cp), sphalerite (sl) and galena (gn) in matrix of saponite, serpentine and clay (2255–5–1P, 11 cm depth; reflected plane-polarized light). Scale bar is 100 μm. (d) Clay-altered talus material, margin of hydrothermal mound, AAV. Very fine grains of pyrite and chalcopyrite rimming rosettes of clay mineral; note nearby diatom (2254–24–1, 5 cm depth; transmitted plane-polarized light). Scale bar is 1 mm. (e) Green-altered hemipelagic sediment proximal to hydrothermal mound, AAV. Fine fragments of collomorphic illite–smectite, clay and Fe-oxides-hydroxides (2254–23–1, 8 cm depth; transmitted plane-polarized light). Scale bar is 1 mm. (f) Green-altered hemipelagic sediment proximal to hydrothermal mound, AAV. Lithic fragments and microfossils (radiolaria, diatoms) in matrix of detrital chlorite, quartz, amphibole, feldspar, mica, and clay. Minor illite–smectite reflects some hydrothermal alteration (2255–5–2, 25 cm depth; transmitted plane-polarized light). Scale bar is 2 mm. (g) Grey-altered hemipelagic sediment distal to hydrothermal mound, AAV. Foraminifera fragments (to 100 μm) in matrix of detrital chlorite, mica, clay, quartz, feldspar, amphibole (2254–22–1, 17 cm depth; transmitted light, crossed polars). Scale bar is 50 μm. (h) Grey-altered hemipelagic sediment distal to hydrothermal mound, AAV. Pyrite framboids within foraminifera test (150 μm) contained in detrital matrix similar to that in Fig. 7g (2254–21–1, 24 cm depth; reflected plane-polarized light). Scale bar is 100 μm.

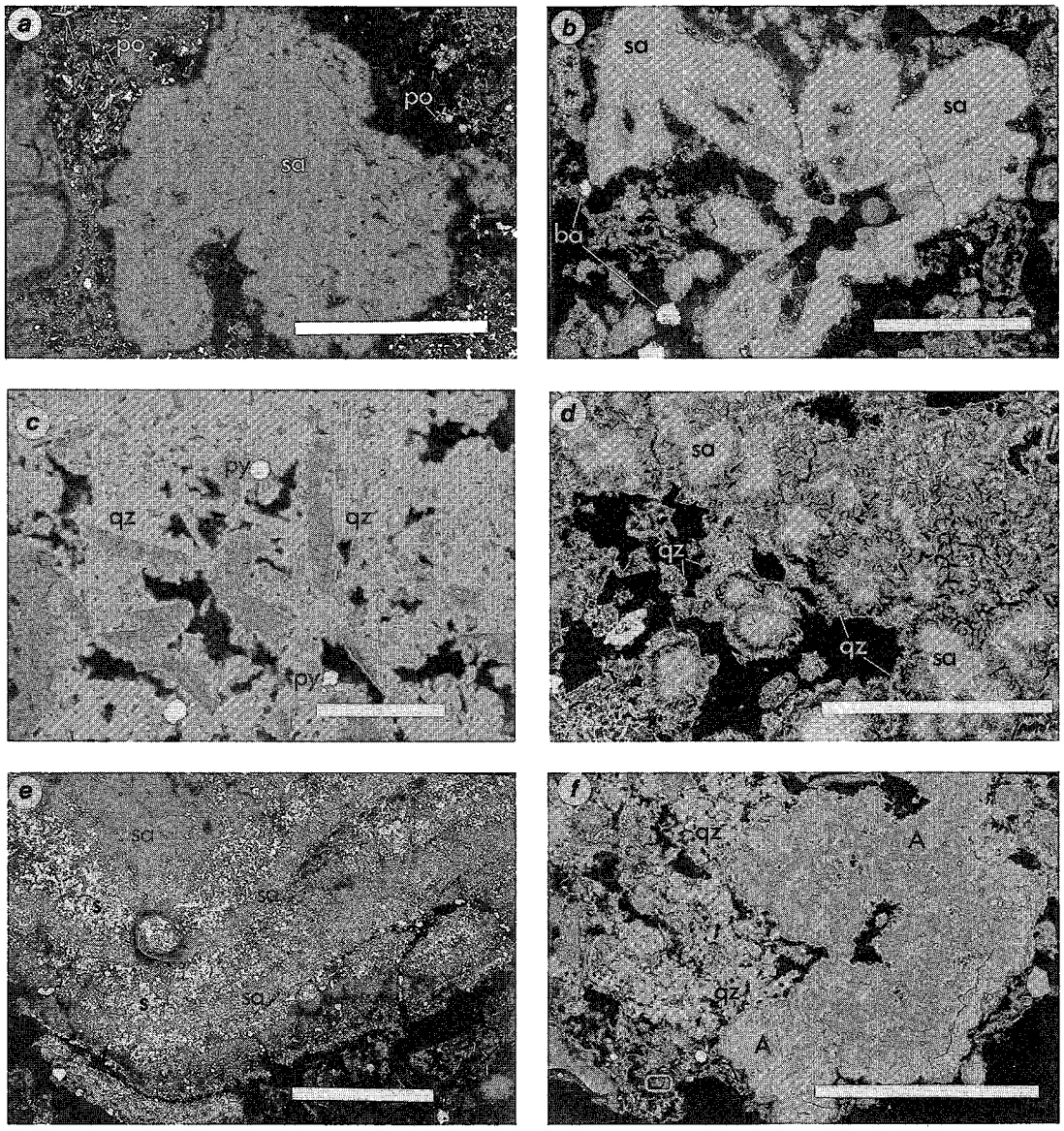

FIG. 6. SEM (secondary electron) photographs of samples from hydrothermal mounds, area of diffuse venting, and adjacent altered sediment. (a) Sulfide-rich layer, hydrothermal mound, Bent Hill area. Coarse anhedral clot of Mg-rich smectite (sa) in fine-grained matrix of Mg-smectite, pyrrhotite laths (po), chalcopyrite, and sphalerite. 2253–1–1, 3–5 cm depth. Scale bar is 200 μm. (b) Green-altered sediment proximal to hydrothermal mound, AAV. Authigenic Mg-rich smectite (sa) as rim and pseudomorph of anhydrite laths, in finer hemipelagic matrix; also includes authigenic barite (ba). 2255–5–2, 23–26 cm depth. Scale bar is 500 μm. (c) Green-altered sediment proximal to hydrothermal mound, AAV. Abundant authigenic quartz (qz) occurs as secondary linings around pores and as replacement of hemipelagic minerals. Note sparse pyrite framboids (py). 2255–5–2, 23–26 cm depth. Scale bar is 50 μm. (d) Green-altered sediment proximal to hydrothermal mound, AAV. Mg-rich clay spheroids (sa) rimmed by fine-grained quartz (qz). 2255–5–2, 23–26 cm depth. Scale bar is 200 μm. (e) Silica–barite-rich silt, area of diffuse venting, AAV. Fragment contains bands of fine sulfides (s), Mg-rich clays (sa), barite and silica. The texture and mineralogy of the fragments are similar to Mg-smectite-lined chimneys from nearby hydrothermal mounds (Ames *et al.* 1993). 2252–2–1, 0–3 cm depth. Scale bar is 200 μm. (f) Silica–barite-rich silt, area of diffuse venting, AAV. Patches of authigenic quartz and lesser magnesian clay (A) without coating of fine-grained quartz (qz). 2252–2–1, 0–3 cm depth. Scale bar is 200 μm.

TABLE 1. RESULTS OF ELECTRON-MICROPROBE ANALYSES OF MAGNESIAN SMECTITE

	Hydrothermal mound		Diffuse vent	Green altered sediment
Core	2255-5-1	2253-1-1	2252-2-1	2255-5-2
N=	9	3	4	3
SiO_2(wt.%)	44.79	51.79	53.68	53.9
Al_2O_3	4.59	1.02	1.1	2.47
Fe_2O_3	1.02	4.12	0	0
FeO	0	0	1.73	1.73
MnO	0.03	0.09	0.12	0.04
MgO	28.91	26.15	25.80	22.29
CaO	0.46	0.22	0.20	0.54
Na_2O	0.69	0.07	0.25	0.15
K_2O	0.16	0.08	0.13	0.19
Total	80.65	83.54	83.01	81.31
$\frac{MgO}{(MgO+SiO_2)}$	0.39	0.34	0.32	0.29
$\frac{Fe}{(Fe+Mg)}$ (Octahedral Site)	0	0.042	0.036	0.042
Calculated Anhydrous Structural Formulae[1] (Basis 22 O, OH)				
Si	6.88	7.63	7.88	8.00
Al	0.83	0.18	0.12	0
Fe^{3+}	0.12	0.20	0	0
	7.82	8.00	8.00	8.00
Al	0	0	0.07	0.31
Fe^{3+}	0	0.26	0	0
Fe^{2+}	0	0	0.21	0.22
Mn	0	0.01	0.01	0.01
Mg	6.62	5.74	5.65	4.97
	6.62	6.01	5.94	5.51
Ca	0.08	0.03	0.03	0.09
Na	0.20	0.02	0.07	0.04
K	0.03	0.02	0.03	0.02
	0.31	0.07	0.13	0.15
Tetrahedral Excess Charge	-1.63	-0.34	-0.12	0
Octahedral Excess Charge	+1.25	+0.28	-0.05	-0.98
Total excess charge	-0.38	-0.06	-0.17	-0.98
Interlayer charge	+0.39	+0.10	+0.16	+0.24

[1] Method of Moore & Reynolds (1989).

TABLE 2. CHEMICAL COMPOSITION OF SAMPLES FROM PUSH CORES

	Diffuse Vent						Mound - Bent Hill						A.A.V. Mound		Talus	Green Altered		
Core	2252-2	2252-2	2252-2	2252-2	2252-2	2252-2	2252-1	2253-1	2253-1	2253-1	2253-1	2253-1	2255-5	2255-5	2254-4	2254-23	2254-23	2254-23
	1	1	1	2	2	2	1	1	1	1	1	1	1	1	1	1	1	1
Interval (cm)	0-5	5-10	10-16	0-7	7-14	14-20	0-4	5-10	10-14	15-20	20-25	25-30	0-8	8-15	0-16	0-4	5-10	10-16
wt. %																		
SiO2	57.50	68.80	79.30	73.10	73.70	49.10	1.23	19.90	43.70	46.30	31.20	25.10	26.50	42.30	51.20	52.40	53.20	52.90
TiO2	0.18	0.16	0.16	0.12	0.10	0.11	0.00	0.03	0.01	0.00	0.02	0.02	0.01	0.04	0.03	0.47	0.51	0.57
Al2O3	4.00	3.70	3.40	2.60	2.20	2.80	0.06	0.85	0.46	0.36	0.62	0.66	1.44	4.76	2.30	9.60	10.40	11.60
Fe2O3t	3.10	3.30	2.90	2.20	2.20	2.50	2.26	42.90	17.40	14.60	30.40	36.60	5.17	1.94	4.90	6.80	6.50	7.10
Fe2O3	N.A.	N.A.	N.A.	N.A.	N.A.	N.A.	N.A.	N.A.	N.A.	N.A.	N.A.	N.A.	N.A.	N.A.	3.00	4.60	2.90	N.A.
FeO	N.A.	N.A.	N.A.	N.A.	N.A.	N.A.	N.A.	N.A.	N.A.	N.A.	N.A.	N.A.	N.A.	N.A.	1.70	2.00	3.20	N.A.
MnO	0.08	0.09	0.08	0.05	0.10	0.34	0.01	0.10	0.04	0.04	0.08	0.05	0.05	0.02	0.13	0.28	0.11	0.10
MgO	8.60	7.61	4.76	5.40	4.45	6.23	0.59	10.00	25.80	27.00	18.30	14.10	12.90	30.60	26.00	11.60	11.30	9.37
CO2	2.22	0.62	0.63	0.52	3.12	16.90	40.10	1.26	0.17	0.08	0.26	0.82	14.20	0.23	0.37	1.62	1.32	1.33
Na2O	1.80	1.60	1.30	1.30	1.00	1.20	0.52	0.65	0.81	0.82	0.86	0.85	1.51	2.82	2.90	2.80	2.80	2.70
K2O	0.66	0.59	0.61	0.49	0.48	0.42	0.04	0.15	0.09	0.08	0.15	0.16	0.20	0.36	0.20	1.33	1.50	1.72
P2O5	0.12	0.07	0.04	0.08	0.03	0.03	0.00	0.18	0.06	0.03	0.11	0.22	0.25	0.05	0.09	0.17	0.14	0.15
C	3.1	1.5	0.6	1.5	0.5	0.5	0.1	0.2	0.1	0.1	0.1	0.2	0.2	0.1	0.4	1.1	1.8	1.7
CO2	1.1	0.1	0.1	N.D.	2.2	13.2	N.D.	N.D.	N.D.	N.D.	N.D.	0.1	N.D.	N.D.	N.D.	0.4	0.1	0.1
H2Ot	N.A.	N.A.	N.A.	N.A.	N.A.	N.A.	N.A.	N.A.	N.A.	N.A.	N.A.	N.A.	N.A.	N.A.	7.7	8.8	8.2	N.A.
S	2.21	2.01	1.28	1.75	1.51	1.35	23.50	23.50	7.84	7.24	19.60	23.50	13.10	1.67	0.89	0.36	0.67	1.32
p.p.m. (wt.)																		
Ba	37000	19000	420	26000	16000	720	1400	18000	590	730	5700	1900	2400	1000	3100	3000	3500	5700
Zn	270	260	180	210	150	160	370	7800	3800	3000	5300	5700	6600	9600	1200	400	390	400
Cu	1900	1700	880	1300	940	1100	1100	22000	6400	4500	17000	25000	19000	6300	6200	1400	1300	1300
Pb	130	150	94	95	170	160	390	190	150	240	100	400	3800	1800	330	220	230	260
Mo	59	35	1	34	19	1	1	55	98	118	84	74	N.D.	N.D.	1	2	6	27
As	46	15	5	23	7	4	5	12	7	12	25	26	N.D.	N.D.	16	11	8	16
Sb	1	1	N.D.	1	1	1	2	1	3	4	14	14	N.D.	N.D.	2	2	2	3
Se	13	7	3	8	4	3	16	7	76	56	233	273	N.D.	N.D.	11	6	7	8
Sr	1300	790	64	1000	640	110	1800	560	36	41	150	97	970	49	310	310	300	380
Rb	17	21	28	15	20	11	N.D.	N.D.	N.D.	N.D.	N.D.	N.D.	N.A.	N.A.	N.D.	46	47	54
Be	1.3	1.1	0.9	1.2	1.1	1.4	0.5	2.1	1.4	1.6	1.5	0.6	0.6	0.1	0.9	1.6	1.7	1.8
Co	6	6	6	5	4	3	N.D.	N.D.	N.D.	N.D.	N.D.	N.D.	9	14	1	13	13	15
Cr	35	26	19	17	6	6	N.D.	N.D.	N.D.	N.D.	N.D.	N.D.	N.D.	N.D.	N.D.	27	33	39
La	3	2	3	1	1	2	N.D.	10	N.D.	N.D.	3	6	N.D.	N.D.	N.D.	13	14	15
Ni	N.D.	N.D.	15	N.D.	N.D.	4	N.D.	N.D.	N.D.	N.D.	N.D.	N.D.	N.D.	11	N.D.	26	N.D.	N.D.
V	61	50	38	46	27	24	N.D.	30	8	7	10	23	12	4	18	98	120	130
Y	4	3	2	2	2	3	3	8	1	N.D.	3	5	N.D.	N.D.	N.D.	15	16	18
Yb	0.7	0.5	0.5	0.4	0.3	N.D.	N.D.	N.D.	N.D.	N.D.	N.D.	N.D.	0.2	N.D.	N.D.	1.5	1.7	1.8
Zr	N.D.	2	18	N.D.	N.D.	9	3	4	N.D.	N.D.	1	1	3	8	N.D.	63	70	78

samples, discussed below, support a limited detrital component in these sediments.

Fine-grained quartz and amorphous silica are abundant and occur as ovoid and anhedral patches up to 1 mm across, as replacement after worm burrows and anhydrite laths, and coating clots of smectite (Figs. 6e, f). Quartz occurs as semimassive anhedral pods. Barite occurs as rosettes, anhedral grains up to 250 μm long, and minor lath-shaped grains up to 2 mm across. Core material also contains gypsum and calcite nodules, and a fragment of a hydrothermal chimney consisting of barite replaced by smectite and sulfides.

Smectite with or without talc occur as patches intergrown with fine-grained quartz (Figs. 6e, f). The smectite differs from those in the hydrothermal mounds by a slightly lower $MgO/(MgO+SiO_2)$ content (Table 2). Clasts of interlayered magnesian smectite and sulfide are similar to material from active chimneys (Fig. 7e; Ames *et al.* 1993). Fine-grained sulfides (<50 μm) occur as disseminations and scattered patches.

GEOCHEMISTRY

The major- and trace-element composition of unaltered hemipelagic sediment (sample 2253–3–1P) is presented in Table 2. Element abundances for this sample are comparable to average values for shallow hemipelagic mud presented for Middle Valley by Goodfellow *et al.* (1993). The contents of chalcophile elements are within the range of average shale (Vine & Tourtelot 1970). Relative to altered sediment, unaltered sediment is distinguished by an elevated content of Ca and CO_2, which reflects significant biogenic carbonate, a low S content bound in diagenetic iron sulfides, a low MgO content that occurs mostly in detrital chlorite, and a low Ba content, likely distributed among carbonate, feldspar and clay minerals.

TABLE 2. CHEMICAL COMPOSITION OF SAMPLES FROM PUSH CORES (Continued)

	Green Altered					Grey Altered								Unaltered			
Core	2254-23	2255-2	2255-2	2255-2	2255-2	2254-21	2254-21	2254-21	2254-21	2254-22	2254-22	2254-22	2254-22	2253-3	2253-3	2253-3	2253-3
	1	2	2	2	2	1	1	1	1	1	1	1	1	1	1	1	1
Interval (cm)	16-23	0-5	5-12	12-22	20-30	0-6	6-12	12-19	19-26	0-8	8-13	13-18	18-23	0-5	5-10	11-17	17-24
wt. %																	
SiO2	52.80	55.20	55.10	52.90	50.20	55.60	56.00	54.60	52.00	54.70	56.00	55.80	55.20	56.70	54.90	54.70	54.50
TiO2	0.66	0.72	0.71	0.64	0.68	0.73	0.77	0.76	0.73	0.73	0.76	0.79	0.78	0.83	0.84	0.86	0.83
Al2O3	13.00	13.70	13.30	12.30	13.00	14.10	15.00	15.40	15.00	13.80	14.60	15.50	16.20	15.50	16.10	16.10	16.10
Fe2O3t	7.40	7.50	7.60	6.90	6.90	7.60	7.40	7.60	7.30	7.60	7.80	7.70	7.90	6.80	6.80	6.90	6.90
Fe2O3	N.A.	5.60	5.20	4.10	N.A.	5.30	4.00	1.70	N.A.	5.50	4.50	3.40	2.00	4.70	3.80	4.10	3.90
FeO	N.A.	1.70	2.20	2.50	N.A.	2.10	3.10	5.30	N.A.	1.90	3.00	3.90	5.30	1.90	2.70	2.50	2.70
MnO	0.09	0.45	0.22	0.09	0.07	0.27	0.08	0.09	0.10	0.48	0.08	0.09	0.09	0.26	0.07	0.06	0.07
MgO	6.48	4.26	4.84	6.43	4.07	3.67	3.69	3.71	3.52	4.10	3.94	3.92	3.86	3.17	3.32	3.29	3.31
CO2	1.54	2.23	2.45	2.20	2.10	2.37	2.45	3.50	5.54	2.03	2.10	2.08	2.15	3.06	5.37	4.97	5.13
Na2O	2.70	2.90	2.80	3.20	3.30	3.20	3.10	3.20	2.80	2.90	3.10	3.00	2.90	3.10	2.60	2.60	2.60
K2O	1.91	1.89	1.86	1.81	2.04	2.01	2.20	2.25	2.19	1.93	2.17	2.31	2.29	2.49	2.50	2.56	2.49
P2O5	0.15	0.21	0.19	0.16	0.16	0.18	0.18	0.17	0.17	0.20	0.17	0.17	0.17	0.20	0.18	0.19	0.18
C	1.5	1.8	1.7	1.5	1.2	1.5	1.2	1.1	1.0	1.6	1.4	1.2	1.2	0.8	0.3	0.3	0.4
CO2	0.1	0.6	0.8	0.6	0.4	0.5	0.5	1.3	2.9	0.5	0.2	0.1	N.D.	1.2	2.8	2.6	2.6
H2Ot	N.A.	7.3	6.8	6.3	N.A.	6.7	6.2	5.8	N.A.	7.1	5.5	5.9	6.4	4.5	3.5	4.9	4.5
S	1.53	0.30	0.28	0.72	1.64	0.29	0.31	0.86	1.06	0.25	0.27	0.36	0.73	0.54	0.12	0.11	0.08
p.p.m. (wt.)																	
Ba	19000	6700	6400	18000	49000	5200	5000	5100	4600	4300	3900	3200	2700	1300	690	690	740
Zn	320	220	240	330	280	220	220	190	190	210	240	220	210	140	120	110	110
Cu	820	590	790	1700	870	140	120	98	82	230	180	130	120	100	110	87	76
Pb	180	190	550	230	42	39	28	28	20	60	50	39	27	29	24	23	19
Mo	31	2	1	1	2	1	8	16	24	3	1	3	15	2	1	1	1
As	12	7	4	3	5	3	3	8	8	5	2	6	10	3	2	3	2
Sb	3	2	1	3	2	1	1	2	2	1	2	2	2	1	1	1	1
Se	6	2	3	6	4	2	2	3	4	2	5	3	4	2	1	1	1
Sr	940	460	450	890	1600	420	420	480	550	380	360	340	330	290	320	290	320
Rb	56	60	64	55	54	73	74	77	74	69	75	84	78	100	100	110	97
Be	1.8	1.8	1.8	1.7	1.7	1.8	1.9	1.8	1.8	1.9	1.9	2	1.9	2.2	2.1	2.2	2.1
Co	16	18	14	12	12	18	17	19	18	20	17	19	19	15	15	15	16
Cr	72	68	53	42	43	59	56	58	68	62	62	77	99	45	47	47	52
La	12	18	17	16	12	18	19	19	18	20	19	22	20	25	24	25	25
Ni	N.D.	N.D.	N.D.	N.D.	N.D.	13	11	N.D.	N.D.	42	64	60	50	53	43	44	44
V	150	120	120	140	130	130	150	160	150	120	160	160	160	120	140	120	120
Y	18	21	20	19	17	20	22	23	22	22	22	23	24	24	25	25	26
Yb	2	2.1	2.1	1.9	1.8	2.1	2.2	2.2	2.1	2.2	2.2	2.3	2.2	2.5	2.4	2.5	2.5
Zr	72	100	95	69	68	110	110	100	95	110	120	120	110	150	140	140	140

N.A. not analyzed; N.D. not detected.

Grey-altered sediment

Grey-altered hemipelagic sediment from these cores contain elevated contents of MgO, total Fe_2O_3, MnO, S, Ba, Zn, Cu, Pb, As, Sb and Se, and are depleted in CaO and CO_2 relative to unaltered sediment (Table 2). The enrichment of the above elements reflects the formation of hydrothermal Mg-rich smectite, barite, pyrite and other sulfides such as sphalerite and chalcopyrite. Plots of Cu *versus* Zn (Fig. 7a) and CaO *versus* MgO (Fig. 7b) show that weakly altered sediment from these cores are enriched in Cu, Zn and MgO, but depleted in CaO if compared to unaltered hemipelagic sediment. Changes in the composition of hydrothermally altered hemipelagic sediment are identical to those documented by Goodfellow *et al.* (1993) in deeper piston-core samples throughout the AAV and Bent Hill areas.

Elements such as Al, Ti and Zr that are expected to behave conservatively during hydrothermal alteration also display an apparent decrease in abundance. A plot of TiO_2 *versus* Al_2O_3 (Fig. 7c), for example, shows this decrease and the high correlation between these elements in both altered and unaltered hemipelagic sediment. The high correlation of TiO_2 with Al_2O_3 is controlled by the association of detrital mica with Ti-bearing minerals in unaltered hemipelagic sediment from Middle Valley. Corresponding decreases of TiO_2 and Al_2O_3 in altered sediment are consistent with their conservative behavior during hydrothermal alteration. The low hydrothermal mobility of these elements and their inverse correlation with hydrothermally contributed elements (*e.g.*, MgO, S and CO_2) indicate that detrital minerals in altered sediment have been diluted by hydrothermal minerals. This is supported by the petrography of altered sediments, which shows that authigenic clays and other hydrothermal minerals have formed in interstices between detrital grains in highly

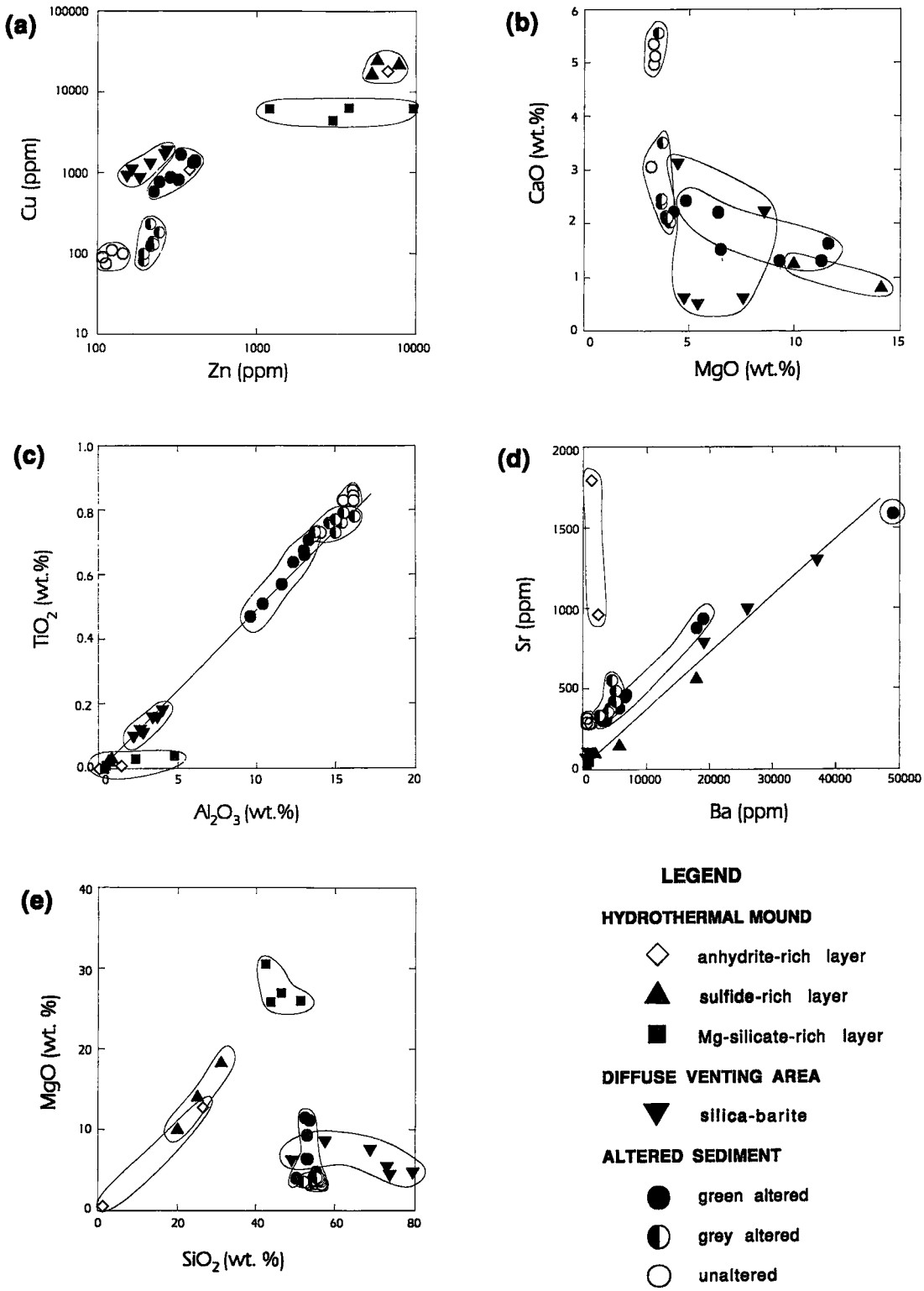
(a)
Cu (ppm)
Zn (ppm)
(b)
CaO (wt.%)
MgO (wt.%)
(c)
TiO2 (wt.%)
Al2O3 (wt.%)
(d)
Sr (ppm)
Ba (ppm)
(e)
MgO (wt. %)
SiO2 (wt. %)
LEGEND
HYDROTHERMAL MOUND
anhydrite-rich layer
sulfide-rich layer
Mg-silicate-rich layer
DIFFUSE VENTING AREA
silica-barite
ALTERED SEDIMENT
green altered
grey altered
unaltered

porous hemipelagic sediment (Goodfellow *et al.* 1993).

Green-altered sediment

The chemical composition of green-altered sediment is similar to grey-altered sediment except that the magnitude of element enrichment or depletion relative to unaltered hemipelagic sediment is greater (Table 2). For example, green-altered sediments contain higher contents of Zn, Cu (Fig. 7a), MgO (Fig. 7b), S, Ba, As, Sb and Se, and are more depleted in CaO (Fig. 7b) and CO_2. The data in Table 2 suggest that during alteration, some Mg may be exchanged with K of a detrital clay precursor phase. However, in some cases, samples plot to the right of the Al–Ti mixing line and confirm growth of new Mg–Al silicates (Fig. 7c). Major and corresponding decreases in TiO_2 and Al_2O_3 (Fig.7c) compared to unaltered hemipelagic sediment suggest that detrital minerals in green-altered sediment have been diluted more than detrital minerals in grey-altered sediment owing to the more extensive infilling of pore space by hydrothermal minerals.

Areas of diffuse hydrothermal discharge

Hydrothermal sediment and hydrothermal chimneys from the area of diffuse hydrothermal discharge are distinguished from hydrothermal products in mounds by higher contents of Ba and SiO_2 (Table 2; Ames *et al.* 1993), and generally lower contents of S and most chalcophile elements. They are enriched, for example, in Cu compared to altered hemipelagic sediment, but depleted in both Zn and Cu relative to hydrothermal sediment on hydrothermal mounds (Fig. 7a). The CaO content is generally lower than values for green-altered sediment, whereas MgO values are similar (Fig. 7b). Samples plot on the TiO_2–Al_2O_3 mixing line between massive sulfides and unaltered hemipelagic sediment, indicating variable but generally minor proportions of hemipelagic sediment (Fig. 7c). The high correlation of Sr with Ba (Fig. 7d) for all samples, except those containing high contents of anhydrite or gypsum, suggests that most of the Sr substitutes for Ba in hydrothermal barite.

Sediment-filled depressions on hydrothermal mounds

The chemical composition of hydrothermal sediment near the summit of the mounds reflects variable proportions of anhydrite and gypsum, Mg-rich silicates, and sulfide minerals, the most important of which are pyrrhotite, pyrite, sphalerite, chalcopyrite and galena. This mineral assemblage is reflected by high contents of S and MgO, that attain 23.5 and 30.6 wt.%, respectively (Table 2). The maximum contents of Zn, Cu and Pb at AAV range up to 0.96, 1.9 and 0.38 wt.%, respectively (Table 2). Values for Cu and Zn, and Cu:Zn ratios (>1) are comparable to those for similar hydrothermal sediment collected in piston and gravity cores from the area (Goodfellow *et al.* 1993), but distinct from massive sulfides at Bent Hill (Cu:Zn = 0.34, Goodfellow *et al.* 1993). The content of Pb, however, is significantly greater in push cores than in piston and gravity cores from AAV and Bent Hill.

Most samples of hydrothermal sediment from mounds display fairly uniform Mg:Si ratios except for samples that contain >20 wt.% MgO (Fig. 6e). The large spread in ratios for high-MgO samples is probably controlled by a mixture of Mg-silicates (*e.g.*, talc) and Mg–Al-silicates. This is evident in Figure 6c for two samples that have a high Al:Ti ratio and plot below the mixing line between detrital and hydrothermal sediments. These samples are distinct from barite–silica hydrothermal sediment taken from areas of diffuse venting, which plot in an area of high silica and low MgO (Fig. 7e).

FIG. 7. Plots of major- and trace-element geochemistry, showing the chemical differences between hydrothermal mound layers (anhydrite–gypsum, sulfide-rich and Mg-silicate-rich), silica–barite hydrothermal sediment, hydrothermally altered detrital sediment (green-altered, grey-altered), and unaltered detrital sediment. (a) Plot of Cu *versus* Zn. (b) Plot of CaO *versus* MgO, showing a systematic decrease of CaO and a corresponding increase in MgO in hydrothermally altered sediment (circles). Also plotted for comparison are samples of hydrothermal sediment. (c) Plot of TiO_2 *versus* Al_2O_3, showing that most samples of hydrothermal sediment and altered sediment fall on a mixing line between unaltered hemipelagic sediment and sulfide-rich layer hydrothermal sediment. The exception are Mg-rich samples from mounds, which fall below the line in the area of high Al:Ti ratios. (d) Plot of Sr *versus* Ba showing that Sr is bound in barite in most samples of altered sediment and hydrothermal sediment, with the exception of anhydrite-rich samples, where Sr probably substitutes for Ca in anhydrite. (e) Plot of MgO *versus* SiO_2, showing that hydrothermal sediment samples from mounds form a linear distribution of fairly uniform Mg:Si ratio. Also plotted for comparison are samples of hydrothermally altered sediment and barite–silica hydrothermal sediment.

Discussion

Comparison with hydrothermal mounds in other sediment-covered rifts

Mound-like hydrothermal deposits have been described in other hydrothermally sediment-covered rifts such as Guaymas Basin, Escanaba Trough, and Hess Basin, Galapagos Rift (*e.g.*, Lonsdale *et al.* 1980, Lonsdale & Becker 1985, Peter & Scott 1988, Honnorez *et al.* 1981, Zierenberg *et al.* in press). These mound structures include low-temperature Fe-rich smectite mounds (T < 50°C) (Honnorez *et al.* 1981), talc–pyrrhotite mounds lacking significant base metals (T ≈ 280°C) (Lonsdale *et al.* 1980) and higher-temperature base-metal-rich sulfide mounds (T > 300°C) (Koski *et al.* 1985, 1988, Peter & Scott 1988).

The best-studied examples of hydrothermal mounds formed in a sediment-covered rift are the base-metal-rich sulfide mounds and talc–pyrrhotite deposits of Guaymas Basin. In the Southern Trough of Guaymas Basin, base-metal-rich sulfide mounds are 5 to 25 m high and 10 to 50 m across, steep-sided, covered by dense mats of tube worms, and characterized by numerous active and inactive spire and chimney structures that vary in height from centimeters to meters. Spires and surface crusts of the mounds are composed of pyrrhotite, sphalerite, wurtzite, galena, isocubanite, chalcopyrite, barite, anhydrite, calcite, aragonite, amorphous silica, talc, and stevensite (Koski *et al.* 1985, Peter & Scott 1988). The maximum temperature measured for vent fluids is 359°C at a seafloor pressure of 200 bars (H. Jannasch, pers. comm. cited in Peter & Scott 1991).

In contrast to the Southern Trough, a large dormant hydrothermal deposit in the Northern Trough of Guaymas Basin appears to lack significant base metal sulfides (Lonsdale *et al.* 1980). Extensive ledges and terraces of ferromanganese-oxide-encrusted white talc with disseminated pyrrhotite and smectite are interpreted as inactive sites of lower-temperature hydrothermal discharge (~280°C) based on estimated temperature of formation of talc from oxygen isotope data (Lonsdale *et al.* 1980). The talc–pyrrhotite deposit occurs on the faulted margin of a small hill underlain by a shallow intrusion and may reflect short-lived expulsions of pore water during sill emplacement.

Similar talc–pyrrhotite aggregates have been described at other sediment-covered spreading centers. At Escanaba Trough, dredge hauls recovered pyrrhotite-rich sulfide slabs with thick (5–10 cm) crusts of massive talc plus minor chlorite and pyrrhotite (Koski *et al.* 1988). In the Galapagos Spreading Center, lithified pelagic turbidite containing talc, smectite, and pyrrhotite was dredged from the floor of Hess deep (Murdmaa & Rozonova 1976).

Whereas massive sulfide mounds in the Guaymas Basin have both focused and diffuse hydrothermal discharge over much of the surface area, AAV mounds have a different hydrologic structure, marked by focused discharge within extensive areas of non-discharge and possibly recharge. In composition, AAV mounds are more similar to the talc–pyrrhotite deposit of the Northern Trough, Guaymas Basin, and the measured temperatures of vent fluids at AAV (240–280°C) are similar to the estimated temperature of formation of the talc–pyrrhotite deposit (280°C). The massive saponite–serpentine and pyrrhotite–pyrite layers intersected in push cores in Middle Valley mounds are likely equivalent to talc–pyrrhotite crusts of the Northern Trough, Guaymas Basin. Based on studies of the mineralogy and geochemistry of hydrothermal chimneys, Ames *et al.* (1993) suggest that the present stage of hydrothermal venting at AAV is both metal- and sulfur-depleted, and the product of low-temperature interaction of seawater-derived hydrothermal fluids with sediments. Extensive coring in AAV by piston and gravity cores (to 12 m depth) (Goodfellow *et al.* 1993) and drilling during Leg 139 of the Ocean Drilling Project (Shipboard Scientific Party 1992c) intersected altered hemipelagic and clay-rich hydrothermal sediments, but did not intersect massive sulfide deposits.

Mg–Fe smectite-rich alteration assemblages

Mg–Fe-silicates display a distinct lateral zonation in and adjacent to hydrothermal mounds (Fig. 8). Based on their nodular form, the white Mg-silicates (saponite, Mg-rich smectite, serpentine, talc) are considered to form *in situ* within hydrothermal mounds. Adjacent to mounds, hemipelagic sediment has a distinctive green color due to the presence of authigenic iron-bearing illite–smectite. *In situ* growth of illite–smectite is indicated by its rosette habit, coarse grain-size, or occurrence of fine-grained clots. Smectite precipitation is favored over chlorite where activity of silica in the hydrothermal fluids is high, as is the case when heated seawater reacts with diatom-rich sediments (Thorton & Seyfried 1987).

Mg-rich silicates such as talc, chlorite, stevensite and smectite are commonly associated with hydrothermal deposits on the seafloor owing to mixing of Mg-bearing seawater with Mg-depleted silica-rich hydrothermal fluids (*e.g.*, Janecky & Seyfried 1984). Uptake of magnesium by secondary phases makes it unlikely that seawater-derived Mg will penetrate into the high-temperature regions of submarine geothermal systems (Seyfried *et al.* 1988). The abundance of saponite and serpentine in the shallow hydrothermal mounds at Middle Valley indicates that significant inflow of seawater occurs through the surfaces of mounds. Lower contents of Mg silicates in surficial sediments adjacent to mounds may result from

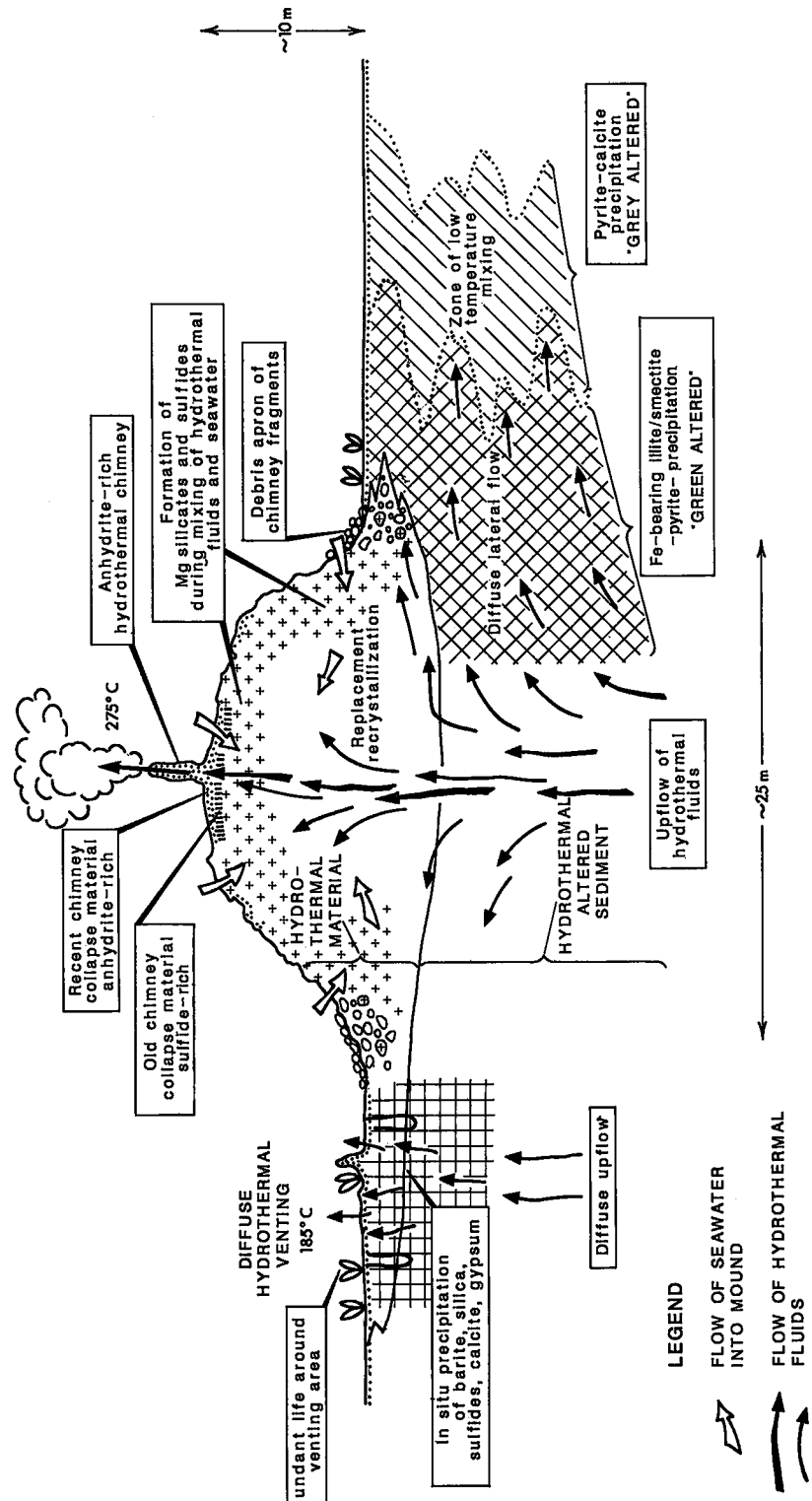

FIG. 8. Schematic figure of hydrothermal mound and adjacent altered sediment, illustrating important processes.

decreased or more diffuse mixing in sediments compared to mounds, or precipitation of Mg-rich silicate at greater depths than the push cores sampled.

The presence of iron-bearing illite–smectite in altered sediment adjacent to mounds likely reflects lower temperatures of formation than for Mg-rich smectite. Zierenberg & Shanks (1988) noted that Mg-rich smectite forms at higher temperatures than Fe-rich smectite (145° to 270°C *versus* 57° to 110°C) within the Atlantis II Deep hydrothermal system in the Red Sea. Dark green nontronite has also formed where low-temperature (19–47°C) hydrothermal fluids interact with calcareous sediments at the Galapagos Mounds area, Galapagos Rift (Barrett *et al.* 1988, McMurtry *et al.* 1983).

Growth of hydrothermal mounds

Push-core samples indicate that chimney growth and collapse contribute at least a veneer of fragmented hydrothermal material to the top of hydrothermal mounds (Fig. 8). Discrete, sharply bounded beds of fragmental anhydrite–gypsum and sulfide – Mg-rich smectite represent debris of fallen chimneys (Turner *et al.* 1991). The lack of oxidation of sulfides in these sediments indicates a high rate of hydrothermal sedimentation. Anhydrite in inactive or collapsed chimneys dissolves rapidly (Johnson & Tunnicliffe 1985); it is likely that the maximum age of the surficial anhydrite–gypsum layers is on the order of weeks. This rapid dissolution of anhydrite suggests that the contribution of anhydrite chimneys to mound growth is likely small unless replacement of anhydrite by clay or barite precedes chimney collapse. Clay-altered chimney fragments are the dominant rubble in the push core that sampled talus flanking a mound.

Some mechanism of expansion and uplift is active within the mounds. Tilted hydrothermal crusts were commonly noted on the surface of hydrothermal mounds, suggesting that a change in internal volume is deforming the rigid crust. Subhorizontal saponite–serpentine veins were intersected in push cores within the lower massive saponite–serpentine layer; these structures can be interpreted either as inflationary "jack-up" features related to fluid overpressures, or as due to thermal dehydration of silicates and volume decrease. It is interesting to note that mound structures of similar dimension to those in Middle Valley in a sediment-filled valley of the Galapagos Rift appear to form exclusively by inflation or uplift, as they lack chimney structures (Honnorez *et al.* 1981, 1983). Cores of these Galapagos mounds contain layers several meters in thickness of coarse granules of Fe-rich smectite that have grown *in situ* within the calcareous ooze that overlie basalt crust (Barrett *et al.* 1988, McMurtry *et al.* 1983).

Origin of sulfide-rich layers

The surficial sediments near the top of a silicate–sulfide mound in the AAV and a massive sulfide mound south of Bent Hill contain the same layers of anhydrite, sulfide and Mg-rich silicate. This similarity suggests that this sediment is related to the current venting of 255–265°C fluids. The sharp contacts between layers and the fragmental nature reflect mass-flow deposition from the collapse of nearby anhydrite chimneys, and dissolution of anhydrite with time (Fig. 8).

Two differing processes are consistent with the character of sulfide-rich beds: they could have formed from the collapse of sulfide-rich chimneys during a period of higher-temperature discharge than at present, or as a residual layer of less-soluble components derived from repeated collapse of anhydrite-rich chimneys similar to those observed. The similarity of Cu:Zn (Fig. 7a) and $MgO:SiO_2$ (Fig. 7e) ratios in anhydrite-rich and sulfide-rich sediment supports the interpretation of a layer of residual sulfide formed by the post-burial dissolution of anhydrite.

Alteration and mineral growth associated with hydrothermal mounds

Active chimneys are composed dominantly of anhydrite, gypsum and bassanite, with a throat lining of Mg-rich smectite + saponite + nontronite, pyrrhotite, pyrite, marcasite, isocubanite, sphalerite, chalcopyrite and galena (Ames *et al.* 1993, Percival & Ames 1993). The presence of gypsum nodules within a chimney toppled by the ALVIN indicates active growth of gypsum; chimney fragments in base-of-mound talus sampled by push core are altered to a clay assemblage that has replaced the original anhydrite. This clay alteration may have occurred *in situ* or prior to collapse of the chimney. The clot-like occurrence of many mineral phases and the presence of nodules and veins indicate alteration and mineral precipitation within the shallow clastic hydrothermal sediments of the mounds. Such *in situ* mineral growth is supported by evidence of elevated temperature of pore water within the hydrothermal mounds (H.P. Johnson, pers. comm., 1990). In the very surficial parts of mounds, disseminated pyrrhotite is widespread and is commonly replaced by pyrite and marcasite, reflecting *in situ* sulfidation. Intergrowths of coarser-grained chalcopyrite, sphalerite and galena with talc and saponite in the deeper parts of cores (>15 cm) may suggest *in situ* precipitation of the base metal sulfides with these magnesian silicates. Galena is distinctly coarser than any noted in active chimneys at Middle Valley (Ames *et al.* 1993).

The lower Mg-rich layer is similar in composition to the overlying sulfide-rich layer, but has a significantly greater ratio of hydrothermal Mg-rich silicates

to sulfides. The Mg-silicate-rich layer also has a higher Al:Ti ratio (Fig. 6c), which suggests that this layer contains a mixture of talc and Mg-rich smectite, whereas talc is the dominant silicate associated with the sulfide-rich layer. Diffuse patches, nodules and subhorizontal veins of saponite, talc and serpentine indicate *in situ* deposition and crystallization of Mg-rich silicates. The abundance of Mg-silicates within the hydrothermal mounds suggests significant flow of seawater into the mounds, presumably driven by entrainment of seawater into the rising hydrothermal fluids within the mounds. Such inflow would account for the low abundance of macroscopic chemosynthetic life on the surface of mounds. The higher fracture-related permeability of the more indurated mound material relative to adjacent clay-rich hemipelagic sediments may account for the higher inflow through mounds (Fig. 8). These data support a model where hydrothermal discharge is narrowly focused at chimneys, and the remainder of the mound surface is a zone of seawater inflow.

Areas of diffuse venting

Hydrothermal venting also occurs by diffuse discharge. The strong H_2S smell of pore fluids in samples recovered from this area and the abundant signs of surface and subsurface biological activity, including clams, mussels, and worms, indicate the diffuse upward flow of sulfide-rich hydrothermal fluids (Fig. 8). A steep temperature-gradient (50°C at 40 cm depth; H.P. Johnson, pers. comm., 1990) exists in the sediments of these areas of diffuse discharge. Although no chimney structures were noted, the abundance of barite, gypsum and sulfide fragments and one large fragment of a small chimney are suggestive of recent chimneys at these vent sites. The boundaries of subsurface layers defined by changes in sulfide content may reflect separate chimney-collapse events and varying temperatures of hydrothermal fluid discharge in the recent past. Alternatively, sulfidic layers also may relate to ponding of hydrothermal fluids and sulfide precipitation below less permeable beds.

The abundance of barite and silica in the surface layers reflects precipitation from rising hydrothermal fluids (Fig. 8). Lydon *et al.* (1990) noted a sharp decrease in the concentration of barium in the surface pore-fluids of the Area of Active Venting and interpreted this to indicate active precipitation of barite near the surface. *In situ* sulfide precipitation is indicated by sulfide-encrusted worm tubes, local clot-like distribution of fine sulfides, and the H_2S-rich nature of pore fluids. The increase of coarser pyrite relative to fine-grained sulfide with depth in samples from the area of diffuse venting area suggests recrystallization and replacement. However, the general decrease in sulfide abundance downhole, sharp changes in sulfide abundance with depth, and generally clastic nature of sulfide grains indicate that the bulk of sulfides are of sedimentary clastic origin. Calcite concretions may represent oxidation of methane in these fluids, as noted elsewhere in the hydrothermal area (Goodfellow & Blaise 1988).

Whether areas of diffuse venting are an early stage of growth of a hydrothermal mound or a distinct form of hydrothermal discharge is unclear (Fig. 8). Crusts of barite- and silica-rich sediment were recovered at the Heineken Hollow site of diffuse venting near an active vent (184°C). The abundance of hydrothermal minerals (barite, silica, sulfide) in the shallow subsurface suggests that areas of diffuse seepage of hydrothermal fluid eventually create impermeable crusts, restrict discharge, and pond hydrothermal fluids below an impermeable cap. Rupture of these caps may result in discharge at discrete centers, prerequisite for the initiation of chimney growth and mound development.

Zoning of silicate–sulfide alteration in hemipelagic sediment

Alteration minerals and textures are zoned about areas of active discharge of hydrothermal fluid (Fig. 8). Hemipelagic sediments adjacent to hydrothermal mounds are sulfide-rich and have a distinctive green color ("green-altered") owing to the abundance of iron-bearing illite–smectite. This iron-bearing illite–smectite assemblage reflects lower temperatures of formation than Mg-rich smectite that dominates mound mineralogy. Smectite abundance decreases with distance from mounds, and chlorite changes from Mg-rich chlorite to Fe–Mg-bearing chlorite.

Farther from mounds but still within the AAV, altered hemipelagic sediment is grey rather than green in color ("grey-altered"), lacks iron-bearing illite–smectite, contains less sulfide, is indurated with calcite cement, and contains carbonate nodules. Although pyrrhotite is partly replaced by pyrite and marcasite in the mounds and proximal sediments, it is absent in distal sediments. Pyrite occurs throughout the AAV, but framboidal pyrite is noted only within distal grey-altered and unaltered hemipelagic sediment. Shallow heat-probe measurements of these sediments indicate marked increases of temperature with depth, suggesting diffuse upward or outward flow of hydrothermal fluids (H.P. Johnson, pers. comm., 1990). Farthest from the mounds, the unaltered sample lacks iron-bearing illite–smectite and carbonate nodules, contains only minor pyrite, and is distinctly less indurated than altered sediments.

ACKNOWLEDGEMENTS

We thank Paul Johnson, Russ McDuff, Bruce Taylor and Rob Zierenberg for many helpful discussions, for sharing their observations on the nature of

the seafloor, and for their involvement in the collection of the push cores. We thank Vee Ann Atnipp for instruction with the core-squeezing apparatus, Mike Black for his help in identifying the biota, and R. Delabio for assistance with XRD analyses. Thanks go also to E. Koopman and M. Tivey, who provided assistance with navigation, the crew of the Atlantis II for their help and hospitality, and the ALVIN pilots for collection of the push cores. Critical reviews by Randy Koski and Roger Bloch significantly improved the manuscript.

REFERENCES

AMES, D.E., HANNINGTON, M.D. & FRANKLIN, J.M. (1993): Mineralogy and geochemistry of active and inactive chimneys and massive sulfide, Middle Valley, northern Juan de Fuca Ridge: an evolving hydrothermal system. *Can. Mineral.* **31**, 997-1024.

BARRETT, T.J., JARVIS, I., LONGSTAFFE, F.J. & FARQUHAR, R. (1988): Geochemical aspects of hydrothermal sediments in the eastern Pacific Ocean: an update. *Can. Mineral.* **26**, 841-858.

DAVIS, E.E., CURRIE, R., SAWYER, B., RIDDIHOUGH, R. & HOLMES, M. (1985): Juan de Fuca Ridge atlas: Seamarc II acoustic image mosaic (northern Juan de Fuca Ridge). *Geol. Surv. Can., Open-File Rep.* **1144**.

———, GOODFELLOW, W.D., BORNHOLD, B.D., ADSHEAD, J., BLAISE, B., VILLINGER, H. & LECHEMINANT, G.M. (1987): Massive sulfides in a sedimented rift valley, northern Juan de Fuca Ridge. *Earth Planet. Sci. Lett.* **82**, 49-61.

——— & LISTER, C.R.B. (1977): Tectonic structures on the Juan de Fuca Ridge. *Geol. Soc. Am. Bull.* **88**, 346-363.

———, MOTTL, M.J. & FISHER, A.T., *et al.* (1992): *Proc. ODP, Init. Reports* . Ocean Drilling Program, College Station, Texas.

GOODFELLOW, W.D. & BLAISE, B. (1988): Sulfide formation and hydrothermal alteration of hemipelagic sediment in Middle Valley, northern Juan de Fuca ridge. *Can. Mineral.* **26**, 675-696.

———, GRAPES, K., CAMERON, B. & FRANKLIN, J.M. (1993): Hydrothermal alteration associated with massive sulfide deposits. Middle Valley, northern Juan de Fuca Ridge. *Can. Mineral.* **31**, 1025-1060.

HONNOREZ, J., KARPOFF, A.M. & TRAUTH-BADAUT, D. (1983): Sedimentology, mineralogy and geochemistry of green clay samples from the Galapagos hydrothermal mounds, Holes 506, 506C, and 507D, Deep Sea Drilling Project Leg 70 (preliminary data). *Initial Reports Deep Sea Drilling Project* **70**, 211-224. U.S. Government Printing Office, Washington, D.C.

———, VON HERZEN, R.P., BARRETT, T.J., BECKER, K., BORELLA, P.E., HUBBERTEN, H.-W., JONES, S.C., KARATO, S., LAVERNE, C., LEVI, S., MIGDISOV, A.A., MOORBY, S.A. & SCHRADER, E.L. (1981): Hydrothermal mounds and young oceanic crust of the Galapagos: preliminary Deep Sea Drilling results, Leg 70. *Geol. Soc. Am. Bull.* **92**, 457-472.

JANECKY, D.R. & SEYFRIED, W.E., JR. (1984): Formation of massive sulfide deposits on oceanic ridge crests: incremental reaction models for mixing between hydrothermal solutions and seawater. *Geochim. Cosmochim. Acta* **48**, 2723-2738.

JOHNSON, H.P., TIVEY, M.A. & FRANKLIN, J.M. (1990): Tectonic control on hydrothermal systems on the northern Juan de Fuca Ridge: Middle Valley and the Endeavour segment. *Trans. Am. Geophys. Union (Eos)* **71**(43), 1566 (abstr.).

——— & TUNNICLIFFE, V. (1985): Time-series measurements of hydrothermal activity on northern Juan de Fuca Ridge. *Geophys. Res. Lett.* **12**, 685-688.

KARSTEN, J.L., HAMMOND, S.R., DAVIS, E.E. & CURRIE, R.G. (1986): Detailed geomorphology and neotectonics of the Endeavor segment, northern Juan de Fuca Ridge: new results from Seabeam swath mapping. *Geol. Soc. Am. Bull.* **97**, 213-221.

KOSKI, R.A., LONSDALE, P.F., SHANKS, W.C., BERNDT, M.E. & HOWE, S.S. (1985): Mineralogy and geochemistry of a sediment-hosted hydrothermal sulfide deposit from the Southern Trough of Guaymas Basin, Gulf of California. *J. Geophys. Res.* **90**, 6695-6707.

———, SHANKS, W.C., III, BOHRSON, W.A. & OSCARSON, R.L. (1988): The composition of massive sulfide deposits from the sediment-covered floor of Escanaba Trough, Gorda Ridge: implications for depositional processes. *Can. Mineral.* **26**, 655-673.

LONSDALE, P. & BECKER, K. (1985): Hydrothermal plumes, hot springs, and conductive heat flow in the Southern Trough of Guaymas Basin. *Earth Planet. Sci. Lett.* **73**, 211-225.

———, BISCHOFF, J.L., BURNS, V.M., KASTNER, M. & SWEENEY, R.E. (1980): A high-temperature hydrothermal deposit on the seabed at a Gulf of California spreading center. *Earth Planet. Sci Lett.* **49**, 8-20.

LYDON, J.W., GOODFELLOW, W.D. & FRANKLIN, J.M. (1990): Geochemistry of pore waters and sediments around active hydrothermal vents, Middle Valley, eastern Pacific Ocean. *Geol. Surv. Can., Current Activities Forum (Ottawa), Program Abstr.*, 20.

———, ——— & GRÉGOIRE, D.C. (1992): Chemical composition of vent and pore fluids in an active hydrothermal discharge zone, Middle Valley. *Geol. Surv. Can., Minerals Colloquium (Ottawa), Program Abstr.*, 7.

MCMURTRY, G.M., WANG, CHUNG-HO & YEH, HSUEH-WEN (1983): Chemical and isotopic investigations into the origin of clay minerals from the Galapagos hydrothermal mounds field. *Geochim. Cosmochim. Acta* **47**, 475-489.

MOORE, D.M. & REYNOLDS, R.C., JR. (1989): *X-Ray Diffraction and the Identification and Analysis of Clay Minerals.* Oxford University Press Inc., New York.

MURDMAA, I.O. & ROZONOVA, T.V. (1976): Hess Deep bottom sediments, in: Geological-geophysical researches in the southeastern part of the Pacific Ocean. Nauka, Moscow, 252-260 (in Russ.).

PERCIVAL, J.B. & AMES, D.E. (1993): Clay mineralogy of active hydrothermal chimneys and associated mounds, Middle Valley, northern Juan de Fuca Ridge. *Can. Mineral.* **31**, 957-971.

PETER, J.M. & SCOTT, S.D. (1988): Mineralogy, composition, and fluid-inclusion microthermometry of seafloor hydrothermal deposits in the Southern Trough of Guaymas Basin, Gulf of California. *Can. Mineral.* **26**, 567-588.

—— & —— (1991): Hydrothermal mineralization in the Guaymas Basin, Gulf of California. *In* The Gulf and Peninsular Province of the Californias (J.P. Dauphin & B.R.T. Simoneit, eds.) *Amer. Assoc. Petrol. Geol., Mem.* **47**, 721-741.

SEYFRIED, W.E., JR., BERNDT, M.E. & SEEWALD, J.S. (1988): Hydrothermal alteration processes at mid-ocean ridges: constraints from diabase alteration experiments, hot-spring fluids, and composition of the oceanic crust. *Can. Mineral.* **26**, 787-804.

SHIPBOARD SCIENTIFIC PARTY (1992a): Introduction. *In* Proc. ODP, Initial Reports **139** (E.E. Davis, M.J. Mottl, A.T. Fisher, *et al.*, eds.) Ocean Drilling Program, College Station, Texas (5-41).

—— (1992b): Site 857. *In* Proc. ODP, Initial Reports **139** (E.E. Davis, M.J. Mottl, A.T. Fisher *et al.*, eds.). Ocean Drilling Program, College Station, Texas (283-427).

—— (1992c): Site 858. *In* Proc. ODP, Initial Reports **139** (E.E. Davis, M.J. Mottl, A.T. Fisher *et al.*, eds.). Ocean Drilling Program, College Station, Texas (431-569).

THORTON, E.C. & SEYFRIED, W.E., JR. (1987): Reactivity of organic-rich sediment in seawater at 350°C, 500 bars: experimental and theoretical constraints and implication for the Guaymas Basin hydrothermal system. *Geochim. Cosmochim. Acta* **51**, 1997-2010.

TURNER, R.J.W., LEITCH, C.H.B., AMES, D.E., HÖY, T., FRANKLIN, J.M. & GOODFELLOW, W.D. (1991): Character of hydrothermal mounds and adjacent altered sediments, active hydrothermal areas, Middle Valley sedimented rift, northern Juan de Fuca Ridge, northeastern Pacific: evidence from ALVIN push cores. *Geol. Surv. Can., Pap.* **91-1E**, 99-108.

VINE, J.D. & TOURTELOT, E.B. (1970): Geochemistry of black shale deposits – a summary report. *Econ. Geol.* **65**, 253-272.

ZIERENBERG, R.A., MORTON, J.L., KOSKI, R.A., ROSS, S.L. & HOLMES, M.L. (in press): Geologic setting of massive sulfide mineralization in the Escanaba Trough. *U.S. Geol. Surv., Bull.*

—— & SHANKS, W.C., III (1988): Isotopic studies of epigenetic features in metalliferous sediment, Atlantis II Deep, Red Sea. *Can. Mineral.* **26**, 737-753.

Received July 2, 1992, revised manuscript accepted September 22, 1993.